Hydrol. Earth Syst. Sci. Discuss., 12, 11905–11957, 2015
www.hydrol-earth-syst-sci-discuss.net/12/11905/2015/
doi:10.5194/hessd-12-11905-2015

Hydrology and Earth System Sciences
Open Access
Discussions

Mapping evapotranspiration with high resolution aircraft imagery over vineyards using one and two source modeling schemes

T. Xia[1,2], W. P. Kustas[2], M. C. Anderson[2], J. G. Alfieri[2], F. Gao[2], L. McKee[2], J. H. Prueger[3], H. M. E. Geli[4], C. M. U. Neale[5], L. Sanchez[6], M. Mar Alsina[6], and Z. Wang[1,7]

[1]Department of Hydraulic Engineering, Tsinghua University, Beijing, 100084, China
[2]USDA-ARS, Hydrology and Remote Sensing Laboratory, Beltsville, MD, USA
[3]USDA-ARS, National Laboratory for Agriculture and the Environment, Ames, IA, USA
[4]Department of Civil and Environmental Engineering, Utah State University, Logan, UT, USA
[5]School of Natural Resources Robert B. Daugherty Water for Food Institute, University of Nebraska–Lincoln, Lincoln, NE, USA
[6]E. & J. Gallo Winery, Viticulture, Chemistry and Enology, Modesto, CA 95353, USA
[7]State Key Laboratory of Hydro-Science and Engineering, Tsinghua University, Beijing, 100084, China

Received: 10 September 2015 – Accepted: 1 October 2015 – Published: 16 November 2015

Correspondence to: W. P. Kustas (bill.kustas@ars.usda.gov)

Published by Copernicus Publications on behalf of the European Geosciences Union.

Abstract

Thermal and multispectral remote sensing data from low-altitude aircraft can provide high spatial resolution necessary for sub-field (≤ 10 m) and plant canopy (≤ 1 m) scale evapotranspiration (ET) monitoring. In this study, high resolution aircraft sub-meter scale thermal infrared and multispectral shortwave data are used to map ET over vineyards in central California with the Two Source Energy Balance (TSEB) model and with a simple model called DATTUTDUT (Deriving Atmosphere Turbulent Transport Useful To Dummies Using Temperature) which uses contextual information within the image to scale between radiometric land surface temperature (T_R) values representing hydrologic limits of potential ET and a non-evaporative surface. Imagery from five days throughout the growing season is used for mapping ET at the sub-field scale. The performance of the two models is evaluated using tower-based energy flux measurements of sensible (H) and latent heat (LE) or ET. The comparison indicates that TSEB was able to derive reasonable ET estimates under varying conditions, likely due to the physically based treatment of the energy and the surface temperature partitioning between the soil/cover crop inter-row and vine canopy elements. On the other hand, DATTUTDUT performance was somewhat degraded presumably because the simple scaling scheme does not consider differences in the two sources (vine and inter-row) of heat and temperature contributions or the effect of surface roughness on the efficiency of heat exchange. Maps of the evaporative fraction ($EF = LE/(H + LE)$) from the two models had similar spatial patterns but different magnitudes in some areas within the fields on certain days. Large EF discrepancies between the models were found on two of the five days (DOY 162 and 219) when there were significant differences with the tower-based ET measurements, particularly using the DATTUTDUT model. These differences in EF between the models translate to significant variations in daily water use estimates for these two days for the vineyards. Model sensitivity analysis demonstrated the high degree of sensitivity of the TSEB model to the accuracy of the T_R data while the DATTUTDUT model was insensitive

HESSD

12, 11905–11957, 2015

as is the case with contextual-based models. However, study domain and spatial resolution will significantly influence the ET estimation from the DATTUTDUT model. Future work is planned for developing a hybrid approach that leverages the strengths of both modeling schemes and is simple enough to be used operationally with high resolution imagery.

1 Introduction

As a key component of the land hydrological, energy and biogeochemical cycles, evapotranspiration (ET) provides important information about terrestrial water availability and consumption (Evett et al., 2012). Detailed knowledge of spatial ET distributions (especially in near-real time) at field or finer scale is particularly useful in precision agricultural water management (Anderson et al., 2012a; Cammalleri et al., 2013; Sánchez et al., 2014). This is especially relevant as the need to increase food production for a growing human population is hindered by the reduced availability of freshwater in many water limited regions, which potentially will be exacerbated with a changing climate. Remote sensing techniques are considered to be one of the few reliable methods for mapping and monitoring ET at watershed and regional scales (Su, 2002; Kustas and Anderson, 2009) since they provide a means for detecting changes in vegetation and soil moisture conditions at field scale affecting ET over space and time.

Over the past several decades, numerous satellite products have been used in ET estimation or monitoring. Among them, medium to moderate spatial resolution (100–1000 m) satellite data, e.g., from Landsat and the MODerate resolution Imaging Spectrometer (MODIS), have been applied with models for ET mapping at field to watershed and regional scales with some success (Anderson et al., 2012b; Cammalleri et al., 2013). (In this paper we define satellite imagery with resolution on order of ~ 100 m as "medium resolution" and 1000 m as "moderate resolution" to distinguish from high resolution imagery with meter-scale spatial resolution.) However, as water resources become more limited, there is a greater need for precision agricultural management at the field/subfield-scale, particularly for high-valued or specialty crops (Zipper and Loheide II, 2014), and moderate resolution data are too coarse to inform variable rate application of water or nutrients within a field. In addition, obtaining both high spatial and temporal resolution data is not feasible with the current satellite constellation since medium resolution earth observations have a long (two or more weeks) revisit cycle, particularly when considering cloud cover (Cammalleri et al., 2013).

Remote sensing data from low altitude aircraft, especially from unmanned aerial vehicles (UAVs), can potentially provide the needed spatial and temporal frequency for precision agriculture applications. Despite the fact that development of airborne scanner-derived thermal imagery for irrigation applications had begun back in the 1970s (Jackson et al., 1977), it is not until the last few years that very high resolution data are being considered for precision agricultural applications. This is due to the technological advances that have allowed rapid integration and processing of high-resolution data from cameras mounted on aircraft and more recently on-board UAVs (Zarco-Tejada et al., 2013). Current applications of high resolution thermal remote sensing data are mainly focused on detecting and mapping crop water status (Berni et al., 2009b; Gonzalez-Dugo et al., 2012; Zarco-Tejada et al., 2012) since canopy temperature has historically been used as an indicator of water stress (Jackson et al., 1981; Gardner et al., 1981; Fuentes et al., 2012). Sub-meter resolution thermal imagery is able to retrieve pure canopy temperature, minimizing soil or other background thermal effects (Leinonen and Jones, 2004; Zarco-Tejada et al., 2013).

Spatially distributed ET can be obtained using remote sensing-based ET models with varying degrees of complexity and utility (Kalma et al., 2008). In terms of treatment of the energy exchange with the surface, the thermal remote sensing-based ET models can be classified as one source (Bastiaanssen et al., 1998; Su, 2002; Feng and Wang, 2013) and two source (Norman et al., 1995; Kustas and Norman, 1999; Long and Singh, 2012; Yang and Shang, 2013) parameterizations depending on whether they

HESSD
12, 11905–11957, 2015

treat a landscape pixel as a composite/lumped surface or explicitly partition energy fluxes and temperatures between soil and vegetation. These models are based on solving the surface energy balance and adopt radiometric surface temperature (T_R) as a key boundary condition (Kustas and Norman, 1996).

A commonly used method in one source models is the contextual scaling approach, which uses T_R and vegetation amount (the normalized difference vegetation index, NDVI, or fractional vegetation cover, f_c) as proxy indicators of ET (Bastiaanssen et al., 1998; Su, 2002; Allen et al., 2007; Carlson et al., 1994; Jiang and Islam, 1999). Accurate identification of extreme hydrologic limits, i.e., potential ET (cold/wet limit) and the largest water stress condition (hot/dry limit), is essential for proper scaling of the surface condition (e.g., the aerodynamic and air temperature difference, dT, and evaporative fraction, EF) of the other pixels between these extremes. Examples include the Surface Energy Balance Algorithm for Land (SEBAL) (Bastiaanssen et al., 1998), the Mapping Evapotranspiration with Internalized Calibration (METRIC) model (Allen et. al., 2007), the triangle model (Carlson et al., 1994), and the satellite-based energy balance algorithm with Reference Dry and Wet limits (REDRAW) (Feng and Wang, 2013).

Zipper and Loheide II (2014) indicated that thermal-based ET models relying on extreme limits are not applicable at sub-field scale (~ 1 m resolutions) since in agricultural landscapes vegetation cover within a field is fairly homogeneous and ideal extreme limits may be difficult to identify, especially during mature crop periods when the canopy is nearly closed. They developed a mixed-input approach combining high resolution airborne and Landsat imagery with local meteorological forcing in a surface energy balance model they called High Resolution Mapping of EvapoTranspiration (HRMET). HRMET combines a two-source modeling approach for estimating available energy between the soil and vegetation elements but uses a single-source scheme for estimating the soil + canopy system H, with LE solved by residual.

On the other hand, the contextual scaling approach can greatly simplify model computations and input data requirements (Carlson, 2007), and can reduce ET retrieval

HESSD
12, 11905–11957, 2015

errors due to bias errors in T_R and meteorological inputs such as air temperature and wind speed (Allen et al., 2007). This facilitates near real-time operational applications for ET monitoring. In the DATTUTDUT (Deriving Atmosphere Turbulent Transport Useful To Dummies Using Temperature) modeling scheme introduced by Timmermans et al. (2015), land surface temperature is the only input needed for ET estimation. DATTUTDUT solves for ET by scaling the evaporative fraction, EF, between the extreme values associated with potential (cool/wet pixel) and zero (hot/dry pixel) ET. Although these types of contextual scaling methods have been tested over a variety of landscapes using mainly moderate resolution remote sensing data, their applicability and performance in retrieving surface fluxes and ET at the high resolution/sub-field scale, and potential problems or behavior at the sub-field scale have not been adequately tested.

The Two Source Energy Balance (TSEB) scheme originally proposed by Norman et al. (1995) and modified by Kustas and Norman (1996, 1999, 2000), has proven to be fairly robust for a wide range of landscape and weather conditions (Li et al., 2005; Kustas and Anderson, 2009; Colaizzi et al., 2012). Unlike single-source models based on contextual scaling approaches, the TSEB model contains a more detailed treatment of the radiative and flux exchange between soil and vegetation elements without the requirement of extreme hydrological limits existing within the scene. Consequently, TSEB is still effective when applied over homogeneous landscapes and environmental conditions.

The performance of TSEB and single-source models using T_R/ET extremes (e.g., SEBAL, METRIC, Trapezoid Interpolation Model (TIM)) has been compared over a corn and soybean region in Iowa during SMACEX (French et al., 2005; Choi et al., 2009), sub-humid grassland and semi-arid rangeland during SGP '97 and Monsoon '90 (Timmermans et al., 2007), as well as a cotton field in Maricopa, Arizona (French et al., 2015). These studies demonstrated that both TSEB and the single-source models can reproduce fluxes with similar agreement to tower-based observations, yet they did reveal significant discrepancies in the ET patterns or spatial distributions

HESSD
12, 11905–11957, 2015

especially in areas with bare soil or sparse vegetation. In general, these model inter-comparisons have mainly used medium resolution satellite imagery such as Landsat and Advanced Spaceborne Thermal Emission and Reflection radiometer (ASTER). French et al. (2015) conducted model comparison using both Landsat and aircraft data, and concluded that daily ET estimation were similar at high and medium spatial resolutions.

The purpose of this paper is to conduct an inter-comparison of TSEB with the very simple contextual-based DATTUTDUT model that can be easily applied operationally using high resolution thermal and multispectral shortwave imagery for sub-field scale ET estimation. The inter-comparison is conducted over two vineyard fields having significantly different biomass in central California. ET estimates from the TSEB and DATTUTDUT models are compared in detail within the contributing source-area of the flux tower in each field, and the spatial patterns of modeled ET are compared throughout the whole vineyard field. Additionally, a sensitivity analysis of key inputs for the two models is conducted providing insight into the potential for precision agricultural water resource management applications using such high resolution earth observations.

2 Model overview

2.1 TSEB model

The TSEB model, developed by Norman et al. (1995), partitions surface temperature and fluxes into soil and vegetation components. Detailed formulations used in TSEB can be found in Kustas and Norman (1999) and Li et al. (2005, 2008). In the TSEB model, the surface energy budgets are balanced for both the soil and canopy components of the scene:

$$R_n = R_{ns} + R_{nc} = H + \mathrm{LE} + G \quad (1)$$

$$R_{ns} = H_s + \mathrm{LE}_s + G \quad (2)$$

$$R_{nc} = H_c + \mathrm{LE}_c \quad (3)$$

where R_n is net radiation ($\mathrm{W\,m^{-2}}$), H is sensible heat flux ($\mathrm{W\,m^{-2}}$), LE is latent heat flux ($\mathrm{W\,m^{-2}}$), and G is soil heat flux ($\mathrm{W\,m^{-2}}$). Subscripts s and c represent the soil and canopy flux components, respectively. T_R is partitioned into component soil, T_s, and canopy temperature, T_c, based on the fractional vegetation cover (f_c):

$$T_R \approx \left[f_c(\theta)T_c^4 + (1 - f_c(\theta))T_s^4\right]^{1/4} \quad (4)$$

where $f_c(\theta)$ is the vegetation cover fraction at the thermal sensor view angle θ. A clumping factor, Ω, is adopted in the $f_c(\theta)$ calculation to account for the row structure of vineyards (i.e., vine biomass concentrated along trellises) using a formulation from Campbell and Norman (1998):

$$f_c(\theta) = 1 - \exp\left[\frac{-0.5\Omega(\theta)\mathrm{LAI}}{\cos(\theta)}\right] \quad (5)$$

where LAI is leaf area index, which is often estimated from NDVI using an empirical LAI ~ NDVI relation (Anderson et al., 2004). When calculating the flux component H, "series" and "parallel" schemes are adopted for the resistance network separately for unstable and stable conditions. Detailed formulations for the two schemes can be found in Norman et al. (1995) and Kustas and Norman (1999). LE_c is initially estimated using a Priestley–Taylor formulation:

$$\mathrm{LE}_c = \alpha_{PT} f_G \frac{\Delta}{\Delta + \gamma} R_{nc} \quad (6)$$

HESSD
12, 11905–11957, 2015

Mapping evapotranspiration with high resolution aircraft imagery

T. Xia et al.

Title Page
Abstract | Introduction
Conclusions | References
Tables | Figures
◀◀ | ▶▶
◀ | ▶
Back | Close
Full Screen / Esc
Printer-friendly Version
Interactive Discussion

where α_{PT} is Priestley–Taylor parameter, which may vary within different vegetation and climate conditions (Norman et al., 1995; Kustas and Norman, 1999; Kustas and Anderson, 2009). In this paper, the initial value of α_{PT} is 1.26. f_G is the LAI fraction that is green with active transpiration. Δ is the slope of the saturation vapor pressure-temperature curve ($\mathrm{Pa\,K^{-1}}$) and γ is the psychrometric constant ($\mathrm{Pa\,K^{-1}}$). G is parameterized as a fraction of R_{ns} by:

$$G = cR_{ns} \tag{7}$$

where c is the empirical coefficient which tends to be constant during midmorning to midday period (Kustas and Anderson, 2009).

With the above model formulations, energy fluxes for both soil and canopy can be solved. Important model inputs for TSEB include T_R, fractional canopy cover condition (often related to NDVI), and a land use map providing canopy characteristics (mainly vegetation height and leaf width) obtained using remote sensing imagery. Ancillary meteorological data required in TSEB include air temperature, vapor pressure, atmospheric pressure, and wind speed.

2.2 DATTUTDUT model

The DATTUTDUT model is an energy balance model that estimates surface energy fluxes solely from radiometric surface temperature observations acquired over the area of interest. This model assumes that T_R is an important indicator for the surface status, and scales key parameters for flux estimation by T_R between the extremes of a cool/wet pixel with ET at the potential rate and hot/dry pixel where there is essentially no ET. Detailed model formulations are described in Timmermans et al. (2015). Similar to other energy balance models, R_n is estimated by computing the net shortwave radiation and the net longwave radiation:

$$R_n = (1-\alpha)S_d + \varepsilon\varepsilon_a\sigma T_a^4 - \varepsilon\sigma T_R^4 \tag{8}$$

HESSD
12, 11905–11957, 2015

where S_d is the downwelling shortwave radiation ($\mathrm{W\,m^{-2}}$), which can be obtained by sun-earth astronomical relationships under clear-sky conditions (Allen et al., 2007; Timmermans et al., 2015), σ is the Stefan–Boltzmann constant ($5.67\times10^{-8}\,\mathrm{W\,m^{-2}\,K^{-4}}$), ε is the broad-band surface emissivity (–) and ε_a is the atmosphere emissivity (–). In the DATTUTDUT model, nominal values are taken for ε and ε_a for simplicity: ε_a is set to be 0.7 and ε is taken as 0.96. Air temperature, T_a (K), is assumed to be equal to the minimum T_R identified within the scene of interest. α is the surface albedo (–), which is scaled with T_R between extreme values of 0.05 and 0.25 based on the assumption that densely vegetated objects are likely to be darker and cooler while bare objects tend to appear brighter and hotter:

$$\alpha = 0.05 + \left(\frac{T_R - T_{min}}{T_{max} - T_{min}}\right)0.2 \tag{9}$$

where T_{max} is the maximum T_R within the image, and T_{min} is the 0.5 % lowest temperature in the scene. Soil heat flux is calculated from R_n with the coefficient c_G scaled between a minimum value of 0.05 for fully covered condition and maximum value of 0.45 for bare soil (Santanello and Friedl, 2003):

$$c_G = \frac{G}{R_n} = 0.05 + \left(\frac{T_R - T_{min}}{T_{max} - T_{min}}\right)0.4 \tag{10}$$

Similar to α and c_G, evaporative fraction, EF, is assumed to be linearly related to T_R:

$$\mathrm{EF} = \frac{\mathrm{LE}}{\mathrm{LE} + H} = \frac{\mathrm{LE}}{R_n - G} = \frac{\mathrm{LE}}{A} = \frac{T_{max} - T_R}{T_{max} - T_{min}} \tag{11}$$

where A is available energy ($\mathrm{W\,m^{-2}}$), i.e., the difference between R_n and G. With the above formulations, LE can be calculated from A and EF, and H can be estimated as the residual to the energy balance equation.

HESSD
12, 11905–11957, 2015

2.3 Daily flux calculation

A common approach used to extrapolate ET from instantaneous to daily time scale is to assume the ratio of instantaneous LE to some reference variable remains constant during the day, which is described as "self-preservation" by Brutsaert and Sugita (1992). The reference variables typically used include A (Anderson et al., 2012b), standardized reference ET (Allen et al., 2007), solar radiation (Zhang and Lemeur, 1995), top-of-atmosphere irradiance (Ryu et al., 2012). Cammalleri et al. (2014) compared the performances of the scale factors derived by these four reference valuables in ET upscaling at 12 AmeriFlux towers, drawing a conclusion that solar radiation was the most robust reference variable for operational applications, particularly in areas where the modeled G component of A may have high uncertainties. However, the applicability of the various reference variables may differ within areas, since energy budget is significantly influenced by surface characteristics such as soil moisture, vegetation condition (Crago, 1996). In this study, EF (defined as the ratio of LE to A or $H+\mathrm{LE}$) is assumed constant during the daytime period when solar radiation is larger than 0. The extrapolation to daytime ET using a constant EF is reasonable to apply during the main growing season period (Cammalleri et al., 2014).

The ratio of instantaneous to daytime A at the flux tower site is used to obtain daytime A for each pixel within the study area by assuming that the A ratio between pixel and flux tower is constant during the daytime. Therefore, daytime A for the pixel ($A_{\mathrm{p,\,d}}$) can be derived from the pixel-based instantaneous A ($A_{\mathrm{p,\,i}}$), and flux tower site values of instantaneous and daytime A ($A_{\mathrm{s,\,i}}$ and $A_{\mathrm{s,\,d}}$) using the following expression:

$$A_{\mathrm{p,\,d}} = \frac{A_{\mathrm{p,\,i}}}{A_{\mathrm{s,\,i}}} A_{\mathrm{s,\,d}} \tag{12}$$

Then daytime ET for each pixel ($\mathrm{ET}_{\mathrm{p,\,d}}$) can be calculated by tower observed daytime A and the EF retrieved by either TSEB or DATTUTDUT:

$$\mathrm{ET}_{\mathrm{p,\,d}} = A_{\mathrm{p,\,d}}\mathrm{EF} \tag{13}$$

HESSD
12, 11905–11957, 2015

and daytime H is computed as the residual in the energy balance equation.

3 Data and site description

3.1 Study site

The model comparison was conducted over two vineyard sites located near Lodi in central California, using data collected as part of the Grape Remote sensing Atmospheric Profiling and Evapotranspiration eXperiment (GRAPEX) (Kustas et al., 2014). With a Mediterranean climate, this area has abundant sunshine and large day-and-night temperature differences, making it a primary wine grape producing area in California. This study focuses on two drip irrigated Pinot Noir vineyards trained on quadrilateral cordons with a 1.5 m space between vines and 3.3 m distance between rows. The north field (Site 1) has an area of about 35 ha with the flux tower located approximately half-way north–south along the eastern border of the field (38°17.3′ N, 121°7.1′ W), while the south vineyard (Site 2) is smaller in size, at about 21 ha with the flux tower also approximately half-way north–south along the eastern border of the field (38°16.8′ N, 121°7.1′ W) (see Fig. 1). The towers were deployed at these locations to maximize fetch for the predominant wind direction during the growing season, which is from the west. The vines in north field (7–8 years old) are more mature than those in south field (4–5 years old), resulting in a greater biomass/leaf area in the north field. Vine height is similar in both fields and reaches ∼ 2.5 m in height. The vines typically leaf out in late March and grow through late August before the grapes are harvested in early September. When winter rains and soil moisture are adequate, a grass cover crop flourishes early in the growing season in the inter-row until becoming senescent starting in late May, which is typically the beginning of the dry season. During the growing season in 2013, the average air temperature was nearly 20 °C and the total precipitation was only about 15 mm.

HESSD
12, 11905–11957, 2015

3.2 Micrometeorological data

Micrometeorological instruments for measuring the meteorological and flux data were installed both in north and south field flux tower sites in late March 2013. The meteorological data needed for running the TSEB model include air temperature, vapor pressure, atmospheric pressure, wind speed, and incoming solar radiation. These were all measured at approximately 5 m above local ground level (a.g.l.) and recorded as 15 min averages. The eddy covariance (EC) system comprised of a Campbell Scientific, Inc.[1] EC150 water vapor/carbon dioxide sensor and a CSAT3 three-dimensional sonic anemometer, both collecting data at 20 Hz producing 15 min averages. A Kipp and Zonen CNR1 four-component radiometer measured net radiation at 6 m a.g.l. Five soil heat flux plates (HFT-3, Radiation Energy Balance Systems, Bellevue, Washington) buried cross-row at a depth of 8 cm recorded soil heat flux. Each heat flux plate had two thermocouples buried at 2 and 6 cm depths and a Stevens Water Monitoring Systems HydraProbe soil moisture sensor buried at a depth of 5 cm used to estimate heat storage above each plate. Both meteorological and fluxes data were measured through the whole vine growing season (April–October) in 2013. During this period (including both daytime and nighttime observations), the slope between A and $H + \mathrm{LE}$ is 0.83 for both two sites with coefficient of determination (R^2) on order of 0.97. This suggests an average energy balance closure of nearly 85 %. In this study, the EC fluxes were closed using both the Residual (RE) and Bowen Ratio (BR) methods described in Twine et al. (2000) to ensure energy conservation.

[1]The use of trade, firm, or corporation names in this article is for the information and convenience of the reader. Such use does not constitute an official endorsement or approval by the United States Department of Agriculture or the Agricultural Research Service of any product or service to the exclusion of others that may be suitable.

HESSD
12, 11905–11957, 2015

3.3 Airborne campaigns

Three Intensive Observation Periods (IOPs) were conducted through the 2013 growing season as part of GRAPEX to capture different vine and inter-row cover crop phenological stages that may affect ET rates. During IOP1 (9–11 April 2013; Day of Year (DOY) 99–101) the vines were just starting to leaf out and the cover crop in the inter-row was green and flourishing. By the time of IOP2 (11–13 June, DOY 162–164), the vines were fully developed with immature green grapes, while the cover crop was senescent. Grapes were beginning to ripen and reach maturity while the vines were still green and growing during IOP3 (6–8 August, DOY 218–220).

Airborne campaigns were conducted on five days (DOY 100, 162, 163, 218 and 219) over the three IOPs. Multispectral and thermal cameras were onboard the Remote Sensing Services Laboratory, Utah State University airborne digital system acquiring images over the two vineyards. This system is installed in a single engine Cessna aircraft dedicated for research. The system consists of three ImperX Bobcat B8430 digital cameras with interference filters forming spectral bands in the green (0.545–0.555 µm), red (0.645–0.655 µm) and near infrared (NIR) (0.780–0.820 µm) wavelengths. The thermal infrared (TIR) images were acquired with a ThermaCAM SC640 by FLIR Systems Inc. in the 7.5–13 µm range. The aircraft-based TIR were provided in degrees Celsius and used in this analysis without performing atmospheric correction. Details of image acquisition and processing can be found in Neale et al. (2012). In Table 1, overpass time (UTC), multispectral and thermal pixel resolution, information and aircraft altitude are listed for the overpass dates. The high spatial resolution of the visible band (0.05 or 0.1 m, see Table 1) made it possible to distinguish vegetation pixels from non-vegetated pixels to some extent. However, with the coarser thermal pixel resolutions it was difficult to reliably distinguish pure vine canopy temperatures from background soil and/or inter-row cover crop temperatures (Fig. 1). Since the imagery for the different overpass dates have different spatial resolutions and the TSEB model resistance and radiation formulations for the turbulent and radiative exchange for the soil/cover-crop-vine system are appropriate at the plot/micrometeorological scale, both multispectral and thermal bands were aggregated to 5 m resolution for creating TSEB input fields to compute ET. This spatial resolution ensured both an inter-row and vine row would be sampled within the pixel. The original 0.38 m resolution thermal imagery fields on DOY163 were also used as input to DATTUTDUT, with some additional sensitivity analysis at higher spatial resolution.

3.4 Model input from aircraft data

The key TSEB model input data from the aircraft observations include maps of NDVI, LAI, f_c, and T_R. Auxiliary remote sensing data were required to produce multispectral reflectance and LAI maps. The original multispectral imagery from aircraft was in digital numbers (DN) and needed to be converted into reflectance. Smith and Milton (1999) introduced an empirical line method to calibrate remote sensing-derived DN to reflectance with errors of only a few percent in their case study. Berni et al. (2009a) applied the empirical line method on high resolution date obtained by UAV yielding calculated reflectances that agreed well with measurements (RMSD = 1.17 %). Since ground-based reflectance measurements were not collected for some of the airborne acquisition dates, Landsat multispectral band reflectance was used to derive the empirical DN ~ reflectance relation for this analysis.

Three Landsat images were used to match the three IOP dates: Landsat 7 on DOY 98 from path44-row33, Landsat 8 on DOY 163 from path43-row33, and Landsat 8 on DOY 218 from path44-row33. Reflectances for Band 5, Band 4, Band 3 from the Landsat 8 images, and Band 4, Band 3, Band 2 from the Landsat 7 image were used to derive the DN ~ reflectance relation of NIR, red, and green band, separately. All shortwave bands were calibrated and atmospherically corrected by the Landsat ecosystem disturbance adaptive processing system (LEDAPS) proposed by Masek et al. (2006).

The DN values with the original aircraft pixel resolution (Table 1) were aggregated up to 30 m resolution to match the Landsat multispectral bands resolution and the

HESSD
12, 11905–11957, 2015

DN ~ reflectance relation was derived. Visible band reflectance measurements were taken during the IOPs on DOY 162, 218 and 219 both above the vine row and over cover crop inter-row for both north and south fields. Estimated NIR, red and green band reflectance at aircraft pixel resolution are compared with reflectance measurements in Fig. 2. Using 54 data points, including the three bands for three days at both sites, estimated reflectance from aircraft data agreed well with observations having a bias (observed-model) of −1.1 % and root mean square difference (RMSD) of 4.5 %. This accuracy is comparable with that (a few percent) found by Smith and Milton (1999) and Berni et al. (2009a).

NDVI was assumed to be correlated with fractional vegetation cover and related to LAI (Carlson and Ripley, 1997). The MODIS Terra four-day composite LAI product (MCD15A3) was used to derive LAI maps at 30 m resolution using the regression tree approach introduced by Gao et al. (2012). NDVI maps were generated from NIR (Band 5) and red (Band 4) band of Landsat 8 data. This permitted the derivation of a LAI ~ NDVI relation at 30 m resolution which was used to create a LAI map at aircraft pixel resolution. An exponential equation was used to fit the LAI ~ NDVI relationship, which was able to accommodate the effect of NDVI saturation at high LAI values (Carlson and Ripley, 1997; Anderson et al., 2004). In Fig. 3, the LAI ~ NDVI equation is compared with ground-based LAI measurements using LiCor LAI-2000 on DOY 163 and DOY 218. The ground-based LAI measurements were derived from 5 transects running due west of the tower at 10–15 m intervals and across 4 rows from south to north. The average LAI from the transects represented a sampling area that was within 75 m due west of the flux tower sites. Four below vine canopy measurements were made and consisted of a LAI observation directly underneath vine plants along a row, and 1/4, 1/2 and 3/4 distance from the vine row.

Values of f_c were derived by the aircraft-based visible bands taking advantage of the high spatial resolution (0.05–0.1 m, see Table 1 and Fig. 1) which allowed separation of the vine canopy from the inter-row area. Pixels were classified into vegetation and non-vegetation categories by ENVI image processing software (Exelis, Boulder, CO), and then the percentage of vegetation pixels was quantified within each 5 m resolution pixel.

4 Results and discussion

4.1 Comparison of model estimates and tower data

Fluxes were modeled by both TSEB and DATTUTDUT at 5 m resolution using the spatially aggregated aircraft-based remotely-sensed observations. TSEB additionally estimates soil and canopy temperatures. A two-dimensional flux footprint model described by Li et al. (2008) based on Hsieh et al. (2000) was used to compute footprint-weighted aggregated model outputs for comparison with the tower-based measurements.

Average soil and canopy component temperatures from TSEB were compared to the aircraft-based observations for the pixels within the flux contributing source area of the towers (Fig. 4). The aircraft-based temperature observations were extracted using a classification of vegetation and non-vegetated areas generated with the high resolution visible bands to identify appropriate pixels in the thermal imagery. The aircraft thermal band had a pixel resolution on the order of 0.5 m (see Table 1), which was often slightly coarser scale than the width of the vine canopy and hence frequently resulted in a mixed pixel, combining both soil and canopy temperatures. Since obtaining a purely vegetated surface temperature observations uncontaminated by background soil or cover crop temperature was difficult given the resolution of the thermal imagery, the minimum of the vegetated temperatures detected within the 5 m pixel was assumed to be a pure vegetated pixel temperature. Then within the footprint source area, the average of the non-vegetated temperatures (assumed to primarily consist of shaded and sunlit areas in the inter-row) was taken as the observed T_s and average of the minimum vegetated temperatures from all 5 m pixels within the source area was estimated to represent the observed T_c. TSEB estimates of T_s and T_c

agreed well with the aircraft thermal observations yielding a bias of 0.5 °C and RMSD on the order of 2.5 °C. This accuracy was comparable with similar types of comparisons reported by Li et al. (2005) and Kustas and Norman (1999, 2000) which had RMSD values ranging from 2.9–4.2 °C for T_s and 1.7–6.4 °C for T_c when comparing observed to TSEB-derived component temperatures.

To assess the utility of the TSEB and DATTUTDUT models in reproducing the observed fluxes from the tower observations in the north (Site 1) and south (Site 2) vineyards, instantaneous modeled fluxes are compared with measurements (adjusted for closure using the RE method) in Fig. 5. Table 2 lists the statistics of model performance compared with both original and adjusted measurements. Since the vines were at the very early growth stage during IOP1, and the inter-row cover crop was the main source of vegetation cover, the observed G on DOY 100 was significantly larger than other IOPs (Fig. 5).

Table 2 clearly shows that the RE closure adjustment method gives better consistency between observed and modeled H and LE for both TSEB and DATTUTDUT in this study. Instantaneous flux from TSEB (H and LE adjusted by RE method) agreed well with obvervation with RMSD ranging between 20 and 60 $\mathrm{W\,m^{-2}}$, which is considered acceptable and similar to prior studies (e.g., Neale et al., 2012). DATTUTDUT gave estimated fluxes with relatively large errors particularly for R_n (RMSD = 66 $\mathrm{W\,m^{-2}}$) and LE (RMSD = 105 $\mathrm{W\,m^{-2}}$) for Site 1. The larger discrepancies in R_n from DATTUTDUT might be attributed to the simplifications in the net radiation computation (see Sect. 2.2). Errors in LE predominantly result from poor performance on DOY 162 and 219 (Fig. 5b and d), likely because the extreme pixels automatically selected on these two days failed to represent the dryest/wettest conditions within the image (see discussion below).

Daytime integrated fluxes are compared with the tower measurements in Fig. 6 and Table 3. Available energy was slightly overestimated by the models for all the cases with biases between −0.5 and −1.4 $\mathrm{MJ\,m^{-2}\,d^{-1}}$. Again, the RE method yielded better agreement with the model estimates of H and LE on a daytime scale. The LE values

HESSD
12, 11905–11957, 2015

from TSEB at Site 1 agreed well with the observations with a bias of 0.5 $MJ\,m^{-2}\,d^{-1}$ and RMSD of 1.1 $MJ\,m^{-2}\,d^{-1}$ (Fig. 6a and Table 3). However LE from DATTUTDUT had larger differences with the measurements at Site 1 (bias = −1.1 $MJ\,m^{-2}\,d^{-1}$ and RMSD = 1.9 $MJ\,m^{-2}\,d^{-1}$) mainly due to the poor agreement in the instantaneous LE. The two models were comparable in their agreement with LE measurements at Site 2 yielding a small bias of −0.5 to ∼ 0 $MJ\,m^{-2}\,d^{-1}$ and for both a RMSD on order of 1.7 $MJ\,m^{-2}\,d^{-1}$.

In general, the TSEB reproduced the measured fluxes with higher accuracy than did DATTUTDUT, both at the instantaneous and daytime temporal scales. It is hypothesized that this likely results from a better physical representation of the energy and radiative exchange within TSEB, since it explicitly considers differences in soil and vegetation radiation and turbulent energy exchange and affects on the radiative temperature source (French et al., 2005; Timmermans et al., 2007). Flux estimation from single-source models based on the use of ET extremes will be sensitive to the selection of extreme end-member T_R pixels (Feng and Wang, 2013; Long and Singh, 2013), and actual extremes might not exist when applying such models to to small vineyards that are uniformly irrigated and managed as in this study. This may be a key factor that caused the fluxes from DATTUTDUT to agree well with measurements on DOY 100, 163 and 218, but not on DOY 162 and DOY 219 when the ET extremes may not have been readily present or captured in the imagery (see discussion below).

In Fig. 7 the locations of the extreme T_R pixels selected according to the DATTUTDUT modeling approach for the five days are shown. The dark green band in the lower half of the south field (especially obvious in Fig. 7b and c) is an old stream bed which is likely to have different soil properties than the surrounding field. For DOY 162 and 219, cold pixels were located at the north vineyard (Fig. 7b and e); while for DOY 163 and 218 just one day later or earlier than DOY 162 and 219, cold pixels were located within this former stream bed or at the tree pixel near the parking lot to the north (Fig. 7c and d). Hot pixels were all located in bare soil pixels near the parking lot or in the north field without vines.

HESSD
12, 11905–11957, 2015

In addition to the issues related to the selection of the T_R end-members, DATTUTDUT does not consider effects of aerodynamic resistance (surface roughness) on the heat exchange for a given surface–air temperature difference. A similar finding was reported by French et al. (2005), where they found bias for H from TSEB was typically within $35\,W\,m^{-2}$, while bias for H from SEBAL could reach up to $150\,W\,m^{-2}$. Nevertheless, the simpler DATTUTDUT modeling scheme is much easier to apply to an image without a priori knowledge or skill required. This is a significant benefit in operational, realtime applications. Moreover as shown by Timmermans et al. (2015), output of fluxes from DATTUTDUT often were in good agreement with flux tower measurements and resulting flux fields had patterns consistent with more physically-based models including TSEB and SEBAL.

4.2 Comparison of spatial patterns in modeled fluxes

Maps of instantaneous EF (assumed to be constant during the day) over the two vineyards are displayed in Fig. 8, along with frequency histograms of daytime ET from the TSEB and DATTUTDUT models expressed in mass units of $mm\,d^{-1}$. During IOP1 (DOY 100), the vines were leafing out in early growth stage and the cover crop in the inter-row was the main source of ET. However, the cover crop in the interrow for the north field was mowed shortly before this aircraft overpass, while the cover crop in the south field was unmowed, and was taller and more lush. As a result, EF and daytime ET distribution histograms showed bimodal shape on DOY 100. The histograms become more unimodal in later IOPs as the vine water use begins to dominate total ET.

While spatial patterns of EF from TSEB and DATTUTDUT were quite similar for all the five overpass dates, driven largely by patterns in T_R (see Fig. 7), the magnitudes in EF differ between the models, some days more significantly than others (Fig. 8a–e). Since the DATTUTDUT model always scales EF between 0 and 1, results from the DATTUTDUT model generally had a wider distribution in EF compared to TSEB. An example of a clear difference in the width of the EF distribution can be seen for DOY 162 in IOP 2 (Fig. 8i), while for daytime ET, differences in the distributions were

HESSD
12, 11905–11957, 2015

quite evident in IOP 2 and IOP 3 (Fig. 8l, n, o). A similar result was obtained by Choi et al. (2009), who compared turbulent fluxes estimated by METRIC, TIM and TSEB using Landsat imagery over a corn and soybean production region in central Iowa.

Despite similar model agreement in instantaneous ET with observations from the tower measurements on DOY 100, 163 and 218 for the three IOPs (Fig. 5), there are in some cases where there are significant differences in maps of EF generated by the two models on these days (Fig. 8). EF discrepancies were particularly large on DOY 162 during IOP2 (Fig. 8b), and on DOY 219 during IOP3 (Fig. 8e). These discrepancies are due primarily to model differences in partitioning A between H and LE within these areas, rather than differences in A itself. Particularly, DATTUTDUT has less sensitivity to dry aerodynamically rough surfaces, which the model does not account for, therefore DATTUTDUT scheme tends to estimate higher EF (Timmermans et al., 2015). Similar spatial discrepancies in model output were reported by Timmermans et al. (2007) and Choi et al. (2009), even though there was good agreement when the models were compared to flux tower measurements. The selection of improper extreme pixels is another crucial factor causing the large discrepancies for the DOY 162 and 219, as analyzed and discussed in Sect. 4.1.

4.3 Sensitivity of TSEB and DATTUTDUT to the key input, T_R

The sensitivity of TSEB and DATTUTDUT model to the key input, T_R, was analyzed in order to further investigate the strengths and weaknesses of the two modeling approaches. The aircraft imagery from DOY 163 was selected as a case study since input data were collected in the afternoon (see Table 1) with near maximum radiation and air temperature conditions. Since T_R is the most important input to both TSEB and DATTUTDUT, EF and ET was calculated with a bias in T_R (±3 °C) to evaluate the sensitivity of these two models to absolute accuracy of T_R. The ±3° bias in T_R was selected based on a comparison between ground-based and the airborne T_R measurements for IOP 3. For DATTUTDUT, the influence of extreme pixel selection on the computed EF and ET was also investigated. Values of EF and ET were also calculated with a 1° deviation in the assigned T_{max}/T_{min} (±1 °C). In addition, the values of T_{max}/T_{min} were selected using the native pixel resolution T_R imagery. Finally, values of T_{max}/T_{min} were derived from imagery encompassing a larger study area/modeling domain both at the aggregated 5 m pixel resolution and the T_R native (∼ 0.6 m) resolution. Note that for TSEB, using finer resolution T_R would not be consistent with the model formulations for partitioning between soil and canopy convective energy and radiation fluxes and kinetic temperatures. A list of sensivity tests conducted, along with the resulting EF and daytime ET statistics describing model output over the north and south vineyards, is provided in Table 4.

Results for the various tests of sensivity of output from TSEB and DATTUTDUT to biases in T_R inputs indicate that the error/uncertainty in EF and ET estimation can be fairly significant for TSEB (Fig. 9a, b, c, l) with an uncertainty in field average ET of ∼ 1 mm d^{-1}, while there is no real impact on the output from DATTUTDUT (Fig. 9d, e, f, m). For TSEB, the shape of the ET distribution remains essentially unchanged, just the mean/centroid of the distribution and max/min ET changed. This result is not unexpected based on prior sensitivity studies of both modeling approaches (e.g., Timmermans et al., 2007). The ±1° change in the max/min T_R also does not impact the output of ET with DATTUTDUT (Fig. 9g, h, n). However, changing the size of the modeling domain for defining max/min T_R and/or the pixel resolution has a measurable impact on the spatially-distributed output from DATTUTDUT in these tests (Fig. 9i, j, k, o). Similar to TSEB, the uncertainty in field average ET is ∼ 1 mm d^{-1}. With a larger study domain, the selected hot pixel is likely to have higher T_R while the cold pixel will tend to have lower T_R (see Table 4) since the number of pixels available for selection of the extremes are increased. This causes the ET estimation from larger domain (Case D5 and D7) to have a narrower distribution compared to ET from smaller domain (Case D0 and D6) (see Fig. 9o). Higher T_R resolution also results in higher hot pixel and lower cold pixel temperatures (Table 4) since the pixels available for extreme selection were more pure and free from the influence of mixed pixel issue. Owing to the different ET potentials for bare soil and vegetation (i.e., bare soil has lower ET while vegetation has

HESSD
12, 11905–11957, 2015

higher ET in this study area), ET estimation from high resolution T_R (Case D6 and D7) tended to be more bimodal than that from lower resolution T_R (Case D0 and D5) (see Fig. 9o).

These tests confirm that simple scaling schemes like DATTUTDUT benefit from insensitivity to biases in T_R, but are sensitive to pixel size and range of conditions present within the modeling domain. This is in contrast to results reported by French et al. (2015), where they concluded that no significant difference in daily ET estimation accuracy was observed running the METRIC model at high (aircraft-based) and medium (Landsat) pixel resolutions. Their study fixed extreme pixels using an objective criteria based on clustered means rather than single pixels, which may reduce the likelihood of an error in selecting an outlier as an extreme hot or cold pixel. Moreover they conducted the inter-comparison of model output at the two resolutions focused on field-averaged ET in comparison to water balance estimates; therefore, the effects on ET distributions or variability were not evaluated in detail. Lastly, the sources of the input data at the two spatial resolutions were provided by the different platforms – aircraft and Landsat; however, the effects of changing the pixel resolution of either the aircraft or satellite data were not evaluated. While more automated approaches are being developed for determining extreme T_R-values in applying contextual-based methods such as METRIC (Morton et al., 2013), the current study demonstrates that pixel resolution of T_R and sampling area will influence the selection of extreme limits in the approach used by DATTUTDUT, resulting in differences in spatial distribution/patterns in ET from DATTUTDUT within a given study area.

4.4 Water consumption analysis

Water consumption estimates at the field scale provide important information for water management decision making. In this section, estimates of field-scale daytime water consumption for the north and south fields were calculated by aggregating daytime ET totals for all pixels encompassed within each field and then converting to a volume (in

HESSD
12, 11905–11957, 2015

liters) by the area of the corresponding field. When using the observed ET (from the flux towers), the field scale water consumption was computed by simply multiplying the tower measured daytime ET (forcing closure by residual) by the area (size) of the vineyard. The volume of water use for each field for the five overpass dates is illustrated in Fig. 10.

The discrepancies between field water consumption from TSEB and DATTUTDUT were relatively small (3–6 %) on DOY 100, 163 and 218, since the instantaneous and daytime ET estimates from the two models were similar. However, the water use estimated from TSEB was 25 and 33 % less than that computed by DATTUTDUT on DOY 162 and 219, respectively. Water consumption calculated by TSEB tended to agree with observed daytime ET estimated from the tower observations, but often had slightly lower ET estimates. This is consistent with the fact that, particularly for the north (Site 1) vineyard, the flux tower footprint generally came from the center area of the field with highest EF and ET (cf. Figs. 1, 8). On the other hand, DATTUTDUT tended to estimate higher field scale ET than TSEB and tower measurements, particularly on DOY 162 and 219. The overall higher estimated water use for IOP2 and IOP3 by DATTUTDUT is likely due to the simplfied parameterization of heat exchange based solely on T_R and the pixel selection criteria for the hydrologic extremes as analyzed in Sects. 4.1 and 4.2.

Water use from TSEB was separated into soil/inter-row evaporation (E) and vine/vegetation transpiration (T) for each day by assuming the E/T ratio estimated at the aircraft overpass time was constant during the daytime period (see the red lines in Fig. 10). The variation of E between days was smaller than the variability in T, with standard deviations in E of 95 and 55 kL for the north and south fields, respectively, as compared 197 and 173 kL for T. On average over the 5 days, the E/ET ratios for site 1 and 2 were estimated by TSEB to be ~ 0.33 and 0.35, respectively. Although observations of E/ET are not available to validate the TSEB estimates of partitioning, other studies in drip-irrigated vineyards report E/ET ratios of $\sim 0.3 \pm 0.12$ (Yunusa et al., 2004; Ferreira et al., 2012; Poblete-Echeverría et al., 2012; Kerridge et al., 2013), indicating TSEB estimates of E/ET partitioning are not unreasonable.

While some level of discrepancy is expected between modeled and measured vineyard water use due to model errors and measurement uncertainties, there are additional factors which may play a role when there appears to be a fairly large difference in water consumption estimated from the tower measurements vs. the models, particularly with the TSEB model which tends to have better agreement with the tower measurements. Specifically, on days like DOY 162 and 163 for the north field and DOY 100 for the south field where there are significant differences between tower observations and TSEB estimates, there are also large differences observed between the LAI within the tower source area and the field average. The lower (higher) LAI of the flux tower source area is associated with the lower (higher) daytime ET estimated from the flux tower observations vs. the spatially-distributed ET output from the TSEB model. The differences in LAI from the source area and field average are not large (see Table 5), but they do support the idea that a single measurement of water use within a vineyard is not always representative of the total vineyard water consumption. In a comparison of ET measurements acquired over irrigated cotton eddy covariance, water balance and lysimeters, Kustas et al. (2015) show how variability in LAI within the different source areas associated with each measurement device was correlated to discrepancies between the measured values ET. In the current study, if the ratio of the field vs. flux tower source area average LAI is used to adjust the water consumption estimates from the ET tower measurements for the two fields, in all cases except one (DOY 100 at Site 2) there is closer agreement with TSEB estimates (see Fig. 10). The continued discrepancy for DOY 100 Site 2 has more to do with the fact that the G values from the tower site were significantly higher than modeled (see Fig. 5) and are suspect since the ratio of G/R_n for much of the daytime period ranged from 0.3 to 0.45 which are values expected for bare soil (Santanello and Friedl, 2003). This resulted in the daytime available energy $R_\mathrm{n} - G$ for the tower site to be ~ 0.7 of the value estimated

HESSD
12, 11905–11957, 2015

by TSEB. Therefore, closure of the tower-based ET flux did not significantly boost the observed value for DOY 100.

With the ET distributions from the models illustrated in Fig. 11, one sees that often the tower measurements fall significantly away from the center/mean of the modeled ET distributions. This is a major advantage with remote sensing-based ET approaches using high pixel resolution data which can capture the actual variation in key surface conditions (vegetation cover, soil moisture) affecting ET. While in most cases the LAI adjustment to the ET tower measurements improved the agreement with model estimated field scale water consumption, the capability of the remote sensing-based surface energy balance models in mapping ET provides a unique tool for identifying areas in the field potentially under water stress conditions. This isn't practical using micrometeorological methods.

5 Discussion and conclusions

High resolution multispectral and thermal imagery obtained by aircraft mounted sensors were used to map evapotranspiration (ET) over two vineyards in central California using both the Two Source Energy Balance (TSEB) and single-source contextual-based DATTUTDUT (Deriving Atmosphere Turbulent Transport Useful To Dummies Using Temperature) model which scales evaporative fraction (EF) between 0 and 1 using only the radiometric surface temperature (T_R) extemes of cold/wet and hot/dry pixels in the remotely sensed scene. This study focused on five aircraft overpass dates (DOY 100, 162, 163, 218 and 219) over the vine growing season in 2013.

Component soil and canopy temperatures from TSEB agreed well with the airborne-based observationsderived within the flux-tower source-area yielding a bias on the order of 0.5 °C and a RMSD-value ∼ 2.5 °C for both soil/cover crop and vine canopy temperatures. Instantaneous and daytime integrated fluxes from the TSEB and DATTUTDUT models were validated with flux tower measurements. The TSEB model

HESSD
12, 11905–11957, 2015

was able to derive satisfactory estimates of both instantaneous and daytime sensible heat flux (H) and latent heat flux (LE) for all the five overpass dates, while overall the DATTUTDUT model output of H and LE were in less agreement with the tower measurements, particualrly for DOY 162 and 219 overpass dates.

Spatial distributions of evaporative fraction, EF, and daytime ET from the two models were compared for all the five overpass dates. While the spatial patterns of relatively high and low values of EF mapped by TSEB and DATTUTDUT for the two vineyard fields were similar, the magnitude and range in the EF values were quite different on certain days. Specifically, the distributions of EF values from DATTUTDUT often yielded a wider range due to the requirement that each image contains ET at the extremes of potential and ET = 0. This resulted in EF and daytime ET magnituides and spatial patterns generated by the two models being fairly similar on DOY 100, 163 and 218, while having larger discrepancies on DOY 162 and 219. In general, inter-comparisons between the performance of TSEB and DATTUTDUT using high resoultion (meter-scale) data tended to yield conclusions consistent with results from prior studies comparing TSEB with single-source models based on contextual scaling of maximum and minimum ET using moderate resolution data (see e.g., French et al., 2005, 2015; Timmermans et al., 2007; Choi et al., 2009). With a more physically-based two-source formulations explicitly treating soil and vegetation energy and radiation exchanges and reliable T_R data, the TSEB model is fairly robust and able to derive reliable ET patterns at sub-field scale under a wide range of environmental conditions. The performance of DATTUTDUT model in computing reliable ET and generating distributions and patterns over the vineyards was similar to TSEB on some of the overpass dates, but for other times the DATTUTDUT model performance was less than satisfactory largely depending on whether there actually existed pixels in the scene that were representative of the extreme ET conditions, namely ET at potential and ET = 0.

Differences in daytime ET estimated from the two models directly contributes to the discrepancies in field-scale water use estimates, which on certain days was quite significant. The discrepancies in field scale water consumption calculations from the

HESSD
12, 11905–11957, 2015

two models ranged from 3 to 33 %, which translated to differences in field scale water use between the two models ranging from approximately 68 000 to 899 000 L. Field-scale water consumption estimated from TSEB agreed more closely with estimates based on tower ET observations, while DATTUTDUT tended to estimate higher water use. Disagreement between modeled and measurements is partly due to the difference with LAI of the tower source area and the whole field average. Larger differences in water use occurred when source area LAI failed to represent the field average. A simple adjustment using the ratio of average LAI from the field and the tower source-area greatly reduced the discrepancy with the TSEB model output. Comparsion between tower measured ET and ET distribution from the models shows that tower measurements generally do not have a value that is representative of the center/mean of the modeled ET distributions.

Compared with water consumption information provided by flux tower observations, the type of spatially-distributed ET information provided by thermal-based energy balance models has clear advantages, particularly when imagery is at high pixel resolution. ET observed by flux tower is sampling a relatively small area of the field, while the ET models with the T_R imagery can provide spatially-distributed water use information over the entire vineyard and consequently identify the spatial distribution of plant water status, a required input for precision irrigation systems. Two-souce schemes like TSEB are able to provide reliable ET estimation as well as the partitioning between E and T since the model explicitly parameterizes the radiative and convective exchanges between the soil and canopy systems.

However, the senstivity analysis indicates that high-quality T_R input data are needed for TSEB. The DATATTUDUT contextual scaling approach, with automatic pixel selection, is not sensitive to errors in T_R and requires only very basic information as model input, making it relatively easy to apply operationally. Nevertheless, such one-source approaches fail to provide estimates of the E and T partitioning, and the ET estimation at least for DATTUTDUT can be sensitive to domain size and spatial resolution due to the simple model parameterizations.

HESSD
12, 11905–11957, 2015

With UAV technology rapidly developing to provide remote sensing products in near real time (Berni et al., 2009a), the DATTUTDUT scheme can provide real time ET maps at sub-field scale that will in many cases yield reliable patterns, but not in all cases appropriate magnitudes in ET. In cases where the landscape is aerodynamically rough and dry, an adjustment to the end-member selection for the DATTUTDUT scheme appears to be necessary (Timmermans et al., 2015). For operational agriculture water resource management applications, stressed conditions or unusual patterns in ET within a field detected by DATTUTDUT should be followed up by running TSEB for these unique cases. If routine high-resolution imagery from UAVs becomes operational, this methodology of first running a very simple ET model (DATTUTDUT) followed by a more robust modeling scehme (TSEB) when there are significant changes in ET patterns detected would help to ensure routine and reliable water use and vegetation stress monitoring for precision agriculture applications.

Acknowledgements. Funding provided by E. & J. Gallo Winery made possible the acquisition and processing of the high resolution aircraft imagery used in this study. In addition we would like to thank the staff of Viticulture, Chemistry and Enology Division of E. & J. Gallo Winery, in particular Nick Dokooozlian, Brent Sams, and Martin Mendez-Costabel who made possible the collection of the field validation data. The author, Ting Xia, acknowledges the US Department of Agriculture for hosting her one-year visit to the Hydrology and Remote Sensing Laboratory, and also the China Scholarship Council (CSC) for financially supporting her stay. This work was also financially supported by the National Natural Science Foundation of China via Grant 51279076 and 91125018, and the Twelfth National Key Science & Technology Program of China via Grant 2013BAB05B03. The US Department of Agriculture (USDA) prohibits discrimination in all its programs and activities on the basis of race, color, national origin, age, disability, and where applicable, sex, marital status, familial status, parental status, religion, sexual orientation, genetic information, political beliefs, reprisal, or because all or part of an individual's income is derived from any public assistance program. (Not all prohibited bases apply to all programs.) Persons with disabilities who require alternative means for communication of program information (Braille, large print, audiotape, etc.) should contact USDA's TARGET Center at (202) 720–2600 (voice and TDD). To file a complaint of discrimination, write to USDA, Director, Office of Civil Rights, 1400 Independence Avenue, S.W., Washington, D.C. 20250-

9410, or call (800) 795-3272 (voice) or (202) 720-6382 (TDD). USDA is an equal opportunity provider and employer.

References

Allen, R. G., Tasumi, M., and Trezza, R.: Satellite-based energy balance for mapping evapotranspiration with internalized calibration (METRIC) – Model, J. Irrig. Drain. E.-ASCE., 133, 380–394, doi:10.1061/(ASCE)0733-9437(2007)133:4(380), 2007.

Anderson, M. C., Neale, C. M. U., Li, F., Norman, J. M., Kustas, W. P., Jayanthi, H., and Chavez, J.: Upscaling ground observations of vegetation water content, canopy height, and leaf area index during SMEX02 using aircraft and Landsat imagery, Remote Sens. Environ., 92, 447–464, doi:10.1016/j.rse.2004.03.019, 2004.

Anderson, M. C., Allen, R. G., Morse, A., and Kustas, W. P.: Use of Landsat thermal imagery in monitoring evapotranspiration and managing water resources, Remote Sens. Environ., 122, 50–65, doi:10.1016/j.rse.2011.08.025, 2012a.

Anderson, M. C., Kustas, W. P., Alfieri, J. G., Gao, F., Hain, C., Prueger, J. H., Evett, S., Colaizzi, P., Howell, T., and Chávez, J. L.: Mapping daily evapotranspiration at Landsat spatial scales during the BEAREX'08 field campaign, Adv. Water Resour., 50, 162–177, doi:10.1016/j.advwatres.2012.06.005, 2012b.

Bastiaanssen, W. G. M., Menenti, M., Feddes, R. A., and Holtslag, A. A. M.: A remote sensing surface energy balance algorithm for land (SEBAL). 1. Formulation, J. Hydrol., 212, 198–212, doi:10.1016/S0022-1694(98)00253-4, 1998.

Berni, J., Zarco-Tejada, P. J., Suárez, L., and Fereres, E.: Thermal and narrowband multispectral remote sensing for vegetation monitoring from an unmanned aerial vehicle, IEEE T. Geosci. Remote, 47, 722–738, doi:10.1109/TGRS.2008.2010457, 2009a.

Berni, J. A. J., Zarco-Tejada, P. J., Sepulcre-Cantó, G., Fereres, E., and Villalobos, F.: Mapping canopy conductance and CWSI in olive orchards using high resolution thermal remote sensing imagery, Remote Sens. Environ., 113, 2380–2388, doi:10.1016/j.rse.2009.06.018, 2009b.

Brutsaert, W. and Sugita, M.: Application of self-preservation in the diurnal evolution of the surface energy budget to determine daily evaporation, J. Geophys. Res.-Atmos., 97, 18377–18382, doi:10.1029/92JD00255, 1992.

HESSD

12, 11905–11957, 2015

Cammalleri, C., Anderson, M. C., Gao, F., Hain, C. R., and Kustas, W. P.: A data fusion approach for mapping daily evapotranspiration at field scale, Water Resour. Res., 49, 4672–4686, doi:10.1002/wrcr.20349, 2013.

Cammalleri, C., Anderson, M. C., and Kustas, W. P.: Upscaling of evapotranspiration fluxes from instantaneous to daytime scales for thermal remote sensing applications, Hydrol. Earth Syst. Sci., 18, 1885–1894, doi:10.5194/hess-18-1885-2014, 2014.

Campbell, G. S. and Norman. J. M.: An Introduction to Environmental Biophysics, Springer-Verlag New York, New York, 1998.

Carlson, T.: An overview of the" Triangle Method" for estimating surface evapotranspiration and soil moisture from satellite imagery, Sensors, 7, 1612–1629, doi:10.3390/s7081612, 2007.

Carlson, T. N. and Ripley, D. A.: On the relation between NDVI, fractional vegetation cover, and leaf area index, Remote Sens. Environ., 62, 241–252, doi:10.1016/S0034-4257(97)00104-1, 1997.

Carlson, T. N., Gillies, R. R., and Perry, E. M.: A method to make use of thermal infrared temperature and NDVI measurements to infer surface soil water content and fractional vegetation cover, Remote Sensing Reviews, 9, 161–173, doi:10.1080/02757259409532220, 1994.

Choi, M., Kustas, W. P., Anderson, M. C., Allen, R. G., Li, F., and Kjaersgaard, J. H.: An intercomparison of three remote sensing-based surface energy balance algorithms over a corn and soybean production region (Iowa, US) during SMACEX, Agr. Forest Meteorol., 149, 2082–2097, doi:10.1016/j.agrformet.2009.07.002, 2009.

Colaizzi, P. D., Kustas, W. P., Anderson, M. C., Agam, N., Tolk, J. A., Evett, S. R., Howell, T. A., Gowda, P. H., and O'Shaughnessy, S. A.: Two-source energy balance model estimates of evapotranspiration using component and composite surface temperatures, Adv. Water Resour., 50, 134–151, doi:10.1016/j.advwatres.2012.06.004, 2012.

Crago, R. D.: Conservation and variability of the evaporative fraction during the daytime, J. Hydrol., 180, 173–194, doi:10.1016/0022-1694(95)02903-6, 1996.

Evett, S. R., Kustas, W. P., Gowda, P. H., Anderson, M. C., Prueger, J. H., and Howell, T. A.: Overview of the bushland evapotranspiration and agricultural remote sensing experiment 2008 (BEAREX08): a field experiment evaluating methods for quantifying ET at multiple scales, Adv. Water Resour., 50, 4–19, doi:10.1016/j.advwatres.2012.03.010, 2012.

HESSD
12, 11905–11957, 2015

Mapping evapotranspiration with high resolution aircraft imagery

T. Xia et al.

Ferreira, M. I., Silvestre, J., Conceição, N., and Malheiro, A. C.: Crop and stress coefficients in rainfed and deficit irrigation vineyards using sap flow techniques, Irrigation Sci., 30, 433–447, doi:10.1007/s00271-012-0352-2, 2012.

Feng, J. and Wang, Z.: A satellite-based energy balance algorithm with reference dry and wet limits, Int. J. Remote Sens., 34, 2925–2946, doi:10.1080/01431161.2012.748990, 2013.

French, A. N., Jacob, F., Anderson, M. C., Kustas, W. P., Timmermans, W., Gieske, A., Su, Z., Su, H., McCabe, M. F., Li, F., Prueger, J., and Brunsell, N.: Surface energy fluxes with the Advanced spaceborne thermal emission and reflection radiometer (ASTER) at the Iowa 2002 SMACEX site (USA), Remote Sens. Environ., 99, 55–65, doi:10.1016/j.rse.2005.05.015, 2005.

French, A. N., Hunsaker, D. J., and Thorp, K. R.: Remote sensing of evapotranspiration over cotton using the TSEB and METRIC energy balance models, Remote Sens. Environ., 158, 281–294, doi:10.1016/j.rse.2014.11.003, 2015.

Fuentes, S., De Bei, R., Pech, J., and Tyerman, S.: Computational water stress indices obtained from thermal image analysis of grapevine canopies, Irrigation Sci., 30, 523–536, doi:10.1007/s00271-012-0375-8, 2012.

Gao, F., Anderson, M. C., Kustas, W. P., and Wang, Y.: Simple method for retrieving leaf area index from Landsat using MODIS leaf area index products as reference, J. Appl. Remote Sens., 6, 063554–1, doi:10.1117/1.JRS.6.063554, 2012.

Gardner, B. R., Blad, B. L., and Watts, D. G.: Plant and air temperatures in differentially-irrigated corn, Agr. Meteorol., 25, 207–217, doi:10.1016/0002-1571(81)90073-X, 1981.

Gonzalez-Dugo, V., Zarco-Tejada, P., Berni, J. A., Suarez, L., Goldhamer, D., and Fereres, E.: Almond tree canopy temperature reveals intra-crown variability that is water stress-dependent, Agr. Forest Meteorol., 154, 156–165, doi:10.1016/j.agrformet.2011.11.004, 2012.

Hsieh, C. I., Katul, G., and Chi, T. W.: An approximate analytical model for footprint estimation of scalar fluxes in thermally stratified atmospheric flows, Adv. Water Resour., 23, 765–772, doi:10.1016/S0309-1708(99)00042-1, 2000.

Jackson, R. D., Reginato, R. J., and Idso, S. B.: Wheat canopy temperature: a practical tool for evaluating water requirements, Water Resour. Res., 13, 651–656, doi:10.1029/WR013i003p00651, 1977.

HESSD
12, 11905–11957, 2015

Mapping evapotranspiration with high resolution aircraft imagery

T. Xia et al.

Jackson, R. D., Idso, S. B., Reginato, R. J., and Pinter, P. J.: Canopy temperature as a crop water stress indicator, Water Resour. Res., 17, 1133–1138, doi:10.1029/WR017i004p01133, 1981.
Jiang, L. and Islam, S.: A methodology for estimation of surface evapotranspiration over large areas using remote sensing observations, Geophys. Res. Lett., 26, 2773–2776, doi:10.1029/1999GL006049, 1999.
Kalma, J. D., McVicar, T. R., and McCabe, M. F.: Estimating land surface evaporation: a review of methods using remotely sensed surface temperature data, Surv. Geophys., 29, 421–469, doi:10.1007/s10712-008-9037-z, 2008.
Kerridge, B. L., Hornbuckle, J. W., Christen, E. W., and Faulkner, R. D.: Using soil surface temperature to assess soil evaporation in a drip irrigated vineyard, Agr. Water Manage., 116, 128–141, doi:10.1016/j.agwat.2012.07.001, 2013.
Kustas, W. and Anderson, M.: Advances in thermal infrared remote sensing for land surface modeling, Agr. Forest Meteorol., 149, 2071–2081, doi:10.1016/j.agrformet.2009.05.016, 2009.
Kustas, W. P. and Norman, J. M.: Use of remote sensing for evapotranspiration monitoring over land surfaces, Hydrolog. Sci. J., 41, 495–516, doi:10.1080/02626669609491522, 1996.
Kustas, W. P. and Norman, J. M.: Evaluation of soil and vegetation heat flux predictions using a simple two-source model with radiometric temperatures for partial canopy cover, Agr. Forest Meteorol., 94, 13–29, doi:10.1016/S0168-1923(99)00005-2, 1999.
Kustas, W. P. and Norman, J. M.: A two-source energy balance approach using directional radiometric temperature observations for sparse canopy covered surfaces, Agron. J., 92, 847–854, doi:10.2134/agronj2000.925847x, 2000.
Kustas, W. P., Anderson, M. C., Prueger, J. H., Alfieri, J. G., McKee, L. G., Xia, T., Sanchez, L., Geli, H., and Neale, C. M. U.: Utility of thermal remote sensing for evapotranspiration estimation of vineyards, in: American Meteorological Society's 31st Conference on Agricultural and Forest Meteorology, Portland, OR, USA, 12–15 May 2014, available at: https://ams.confex.com/ams/31AgF2BioGeo/webprogram/Paper246963.html, last access: 16 October 2015, 2014.
Kustas, W. P., Alfieri, J. G., Evett, S., and Agam, N.: Quantifying variability in field-scale evapotranspiration measurements in an irrigated agricultural region under advection, Irrigation Sci., 33, 325–338, doi:10.1007/s00271-015-0469-1, 2015.

Leinonen, I. and Jones, H. G.: Combining thermal and visible imagery for estimating canopy temperature and identifying plant stress, J. Exp. Bot., 55, 1423–1431, doi:10.1093/jxb/erh146, 2004.

Li, F., Kustas, W. P., Prueger, J. H., Neale, C. M., and Jackson, T. J.: Utility of remote sensing-based two-source energy balance model under low-and high-vegetation cover conditions, J. Hydrometeorol., 6, 878–891, doi:10.1175/JHM464.1, 2005.

Li, F., Kustas, W. P., Anderson, M. C., Prueger, J. H., and Scott, R. L.: Effect of remote sensing spatial resolution on interpreting tower-based flux observations, Remote Sens. Environ., 112, 337–349, doi:10.1016/j.rse.2006.11.032, 2008.

Long, D. and Singh, V. P.: A two-source trapezoid model for evapotranspiration (TTME) from satellite imagery, Remote Sens. Environ., 121, 370–388, doi:10.1016/j.rse.2012.02.015, 2012.

Long, D. and Singh, V. P.: Assessing the impact of end-member selection on the accuracy of satellite-based spatial variability models for actual evapotranspiration estimation, Water Resour. Res., 49, 2601–2618, doi:10.1002/wrcr.20208, 2013.

Masek, J. G., Vermote, E. F., Saleous, N. E., Wolfe, R., Hall, F. G., Huemmrich, K. F., Gao, F., Kutler, J., and Lim, T. K.: A Landsat surface reflectance dataset for North America, 1990–2000, IEEE Geosci. Remote S., 3, 68–72, doi:10.1109/LGRS.2005.857030, 2006.

Morton, C. G., Huntington, J. L., Pohll, G. M., Allen, R. G., McGwire, K. C., and Bassett, S. D.: Assessing calibration uncertainty and automation for estimating evapotranspiration from agricultural areas using METRIC, J. Am. Water. Resour. As., 49, 549–562, doi:10.1111/jawr.12054, 2013.

Neale, C. M., Geli, H. M. E., Kustas, W. P., Alfieri, J. G., Gowda, P. H., Evett, S. R., Prueger, J. H., Hipps, L. E., Dulaney, W. P., Chavez, J. L., French, A. N., and Howell, T. A.: Soil water content estimation using a remote sensing based hybrid evapotranspiration modeling approach, Adv. Water Resour., 50, 152–161, doi:10.1016/j.advwatres.2012.10.008, 2012.

Norman, J. M., Kustas, W. P., and Humes, K. S.: Source approach for estimating soil and vegetation energy fluxes in observations of directional radiometric surface temperature, Agr. Forest Meteorol., 77, 263–293, doi:10.1016/0168-1923(95)02265-Y, 1995.

Poblete-Echeverría, C., Ortega-Farias, S., Zuñiga, M., and Fuentes, S.: Evaluation of compensated heat-pulse velocity method to determine vine transpiration using combined measurements of eddy covariance system and microlysimeters, Agr. Water Manage., 109, 11–19, doi:10.1016/j.agwat.2012.01.019, 2012.

HESSD

12, 11905–11957, 2015

Ryu, Y., Baldocchi, D. D., Black, T. A., Detto, M., Law, B. E., Leuning, R., Miyata, A., Reichstein, M., Vargas, R., Ammann, C., Beringer, J., Flanagan, L., Gu, L. H., Hutley, L. B., Kim, J., McCaughey, H., Moors, E. J., Rambal, S., and Vesala, T.: On the temporal upscaling of evapotranspiration from instantaneous remote sensing measurements to 8-day mean daily-sums, Agr. Forest Meteorol., 152, 212–222, doi:10.1016/j.agrformet.2011.09.010, 2012.

Santanello Jr, J. A. and Friedl, M. A.: Diurnal covariation in soil heat flux and net radiation, J. Appl. Meteorol., 42, 851–862, doi:10.1175/1520-0450(2003)042<0851:DCISHF>2.0.CO;2, 2003.

Sánchez, L., Mendez-Costabel, M., Sams, B., Morgan, A., Dokoozlian, N., Klein, L. J., Hinds, N., Hamann, H. F., Claassen, A., and Lew, D.: Effect of a variable rate irrigation strategy on the variability of crop production in wine grapes in California, 12th International Conference on Precision Agriculture, Sacramento, CA, USA, 20–23 July 2014, available at: https://www.ispag.org/presentation/3/1582/, last access: 30 July 2015, 2014.

Smith, G. M. and Milton, E. J.: The use of the empirical line method to calibrate remotely sensed data to reflectance, Int. J. Remote Sens., 20, 2653–2662, doi:10.1080/014311699211994, 1999.

Su, Z.: The Surface Energy Balance System (SEBS) for estimation of turbulent heat fluxes, Hydrol. Earth Syst. Sci., 6, 85–100, doi:10.5194/hess-6-85-2002, 2002.

Timmermans, W. J., Kustas, W. P., Anderson, M. C., and French, A. N.: An intercomparison of the surface energy balance algorithm for land (SEBAL) and the two-source energy balance (TSEB) modeling schemes, Remote Sens. Environ., 108, 369–384, doi:10.1016/j.rse.2006.11.028, 2007.

Timmermans, W. J., Kustas, W. P., and Andreu, A.: Utility of an automated thermal-based approach for monitoring evapotranspiration, Acta Geophys., doi:10.1515/acgeo-2015-0016, online first, 2015.

Twine, T. E., Kustas, W. P., Norman, J. M., Cook, D. R., Houser, P., Meyers, T. P., Prueger, J. H., Starks, P. J., and Wesely, M. L.: Correcting eddy-covariance flux underestimates over a grassland, Agr. Forest Meteorol., 103, 279–300, doi:10.1016/S0168-1923(00)00123-4, 2000.

Yang, Y. and Shang, S.: A hybrid dual-source scheme and trapezoid framework–based evapotranspiration model (HTEM) using satellite images: algorithm and model test, J. Geophys. Res.-Atmos., 118, 2284–2300, doi:10.1002/jgrd.50259, 2013.

Yunusa, I. A. M., Walker, R. R., and Lu, P.: Evapotranspiration components from energy balance, sapflow and microlysimetry techniques for an irrigated vineyard in inland Australia, Agr. Forest Meteorol., 127, 93–107, doi:10.1016/j.agrformet.2004.07.001, 2004.

Zarco-Tejada, P. J., González-Dugo, V., and Berni, J. A.: Fluorescence, temperature and narrow-band indices acquired from a UAV platform for water stress detection using a micro-hyperspectral imager and a thermal camera, Remote Sens. Environ., 117, 322–337, doi:10.1016/j.rse.2011.10.007, 2012.

Zarco-Tejada, P. J., González-Dugo, V., Williams, L. E., Suárez, L., Berni, J. A., Goldhamer, D., and Fereres, E.: A PRI-based water stress index combining structural and chlorophyll effects: assessment using diurnal narrow-band airborne imagery and the CWSI thermal index, Remote Sens. Environ., 138, 38–50, doi:10.1016/j.rse.2013.07.024, 2013.

Zhang, L. and Lemeur, R.: Evaluation of daily evapotranspiration estimates from instantaneous measurements, Agr. Forest Meteorol., 74, 139–154, doi:10.1016/0168-1923(94)02181-I, 1995.

Zipper, S. C. and Loheide II, S. P.: Using evapotranspiration to assess drought sensitivity on a subfield scale with HRMET, a high resolution surface energy balance model, Agr. Forest Meteorol., 197, 91–102, doi:10.1016/j.agrformet.2014.06.009, 2014.

Table 1. Flight and pixel resolution information concerning the images obtained from the airborne campaigns.

IOP	Date (DOY)	Flight time (UTC)	Original spatial resolution (m)		Flight height (m)
			Multispectral	Thermal	
1	10 Apr (100)	18:29–18:43	0.09	0.7	430
2	11 Jun (162)	18:20–18:26	0.05	0.42	240
2	12 Jun (163)	21:11–21:16	0.05	0.38	240
3	6 Aug (218)	18:34–18:37	0.1	0.66	480
3	7 Aug (219)	18:46–18:49	0.1	0.65	480

HESSD
12, 11905–11957, 2015

Table 2. Statistics describing comparisons between modeled fluxes from TSEB and DATTUTDUT at the overpass time and observations (original and with adjustments using the RE and BR methods for energy balance closure) ($W m^{-2}$).

Site	Flux	Day No.	Mean Obs.	TSEB			DATTUTDUT		
				Bias	MAE	RMSD	Bias	MAE	RMSD
Site 1	R_n	5	593	0	26	33	−43	64	66
	G	5	85	5	28	33	−18	35	40
	H	5	195	13	37	42	48	53	68
	LE	5	268	−63	70	87	−117	117	150
	LE_{RE}	5	313	−18	32	37	−73	76	105
	H_{BR}	5	215	33	55	62	68	71	89
	LE_{BR}	5	293	−38	50	58	−92	94	125
Site 2	R_n	5	590	6	15	23	−19	26	27
	G	5	132	41	43	59	6	47	61
	H	4	195	−23	43	45	8	31	39
	LE	4	186	−90	90	102	−106	106	119
	LE_{RE}	4	253	−23	43	51	−38	55	63
	H_{BR}	4	231	13	33	48	44	59	68
	LE_{BR}	4	217	−59	61	77	−74	77	93

HESSD
12, 11905–11957, 2015

Table 3. Statistics describing comparisons between modeled daytime fluxes from TSEB and DATTUTDUT model and observations (original and with adjustments using the RE and BR methods) ($MJ\,m^{-2}\,d^{-1}$).

Site	Flux	Day No.	Mean Obs.	TSEB			DATTUTDUT		
				Bias	MAE	RMSD	Bias	MAE	RMSD
Site 1	$R_n - G(A)$	5	15.0	−0.5	0.7	0.9	−1.2	1.2	1.5
	H	5	4.4	−1.0	1.2	1.4	−0.1	1.0	1.2
	LE	5	8.5	−1.6	1.6	1.8	−3.2	3.2	3.6
	LE_{RE}	5	10.6	0.5	1.0	1.1	−1.1	1.4	1.9
	H_{BR}	5	9.9	4.4	4.4	5.1	5.4	5.4	6.1
	LE_{BR}	5	5.1	−4.9	4.9	5.4	−6.6	6.6	7.1
Site 2	$R_n - G(A)$	5	13.9	−1.4	1.5	1.9	−1.1	1.5	2.3
	H	4	5.2	−1.8	1.8	2.2	−0.8	1.1	1.3
	LE	4	6.2	−2.6	2.6	2.9	−3.1	3.1	3.5
	LE_{RE}	4	8.8	0.0	1.7	1.7	−0.5	1.7	1.8
	H_{BR}	4	7.6	0.6	1.9	1.9	1.6	1.6	1.8
	LE_{BR}	4	6.4	−2.4	3.0	3.4	−2.9	2.9	3.4

HESSD
12, 11905–11957, 2015

Table 4. Statistics describing EF and daytime ET produced by TSEB and DATTUTDUT over the north and south vineyards for each sensitivity test described in the text.

Model	Cases	Input setting	T_R of extreme limits (°C) T_{max}	T_{min}	EF Mean[1]	Med.[2]	SD[3]	Max.[4]	Min.[5]	Daytime ET (mm) Mean	Med.	SD	Max.	Min.
TSEB	Case T0	Original Input	–	–	0.61	0.62	0.12	0.91	0.01	4.3	4.4	1.0	6.8	0.1
	Case T1	$T_R + 3$	–	–	0.46	0.48	0.14	0.80	0.02	3.2	3.3	1.1	5.9	0.1
	Case T2	$T_R - 3$	–	–	0.73	0.74	0.11	0.99	0.02	5.3	5.3	1.0	7.6	0.1
DATTUTDUT	Case D0	Original Input	54.7	31.4	0.67	0.67	0.11	1	0	4.5	4.5	1.3	8.9	0
	Case D1	$T_R + 3$	57.7	34.4	0.67	0.67	0.11	1	0	4.4	4.3	1.2	8.7	0
	Case D2	$T_R - 3$	51.7	28.4	0.67	0.67	0.11	1	0	4.7	4.6	1.3	9.1	0
	Case D3	$T_{max} + 1$	55.7	31.4	0.68	0.68	0.11	1	0.04	4.7	4.6	1.2	8.9	0.1
	Case D4	$T_{min} - 1$	54.7	30.4	0.64	0.64	0.11	0.96	0	4.3	4.2	1.2	8.3	0
	Case D5	Whole Area	58.4	23.4	0.55	0.55	0.08	0.77	0.11	3.4	3.3	0.8	5.9	0.3
	Case D6	Native Resolution	58.5	25.7	0.62	0.64	0.17	1	0	4.2	4.2	1.8	9.3	0
	Case D7	Whole Area and Native Resolution	61.4	20.3	0.57	0.58	0.13	0.87	0.07	3.6	3.6	1.4	7.4	0.2

[1] Mean: mean of the EF or ET distribution,
[2] Med.: median of the EF or ET distribution,
[3] SD: standard deviation of the EF or ET distribution,
[4] Max.: maximum value of the EF or ET distribution,
[5] Min.: minimum value of the EF or ET distribution.

HESSD
12, 11905–11957, 2015

HESSD
12, 11905–11957, 2015

Table 5. Average leaf area index (LAI) estimated for the flux tower source area/flux footprint vs. the whole field derived from the aircraft imagery (NDVI relationship with LAI). The LAI values in bold are associated with the days where differences in water consumption estimated by TSEB vs. using the tower measured ET are significant for Site 1 (North vineyard) and Site 2 (South vineyard).

Site	DOY	LAI	
		Source Area	Whole Field
1	100	1.3	1.3
	162	**2.0**	**1.5**
	163	**1.8**	**1.5**
	218	1.6	1.5
	219	1.7	1.5
2	100	**1.7**	**1.9**
	162	1.5	1.5
	163	1.5	1.5
	218	1.2	1.2
	219	1.3	1.2

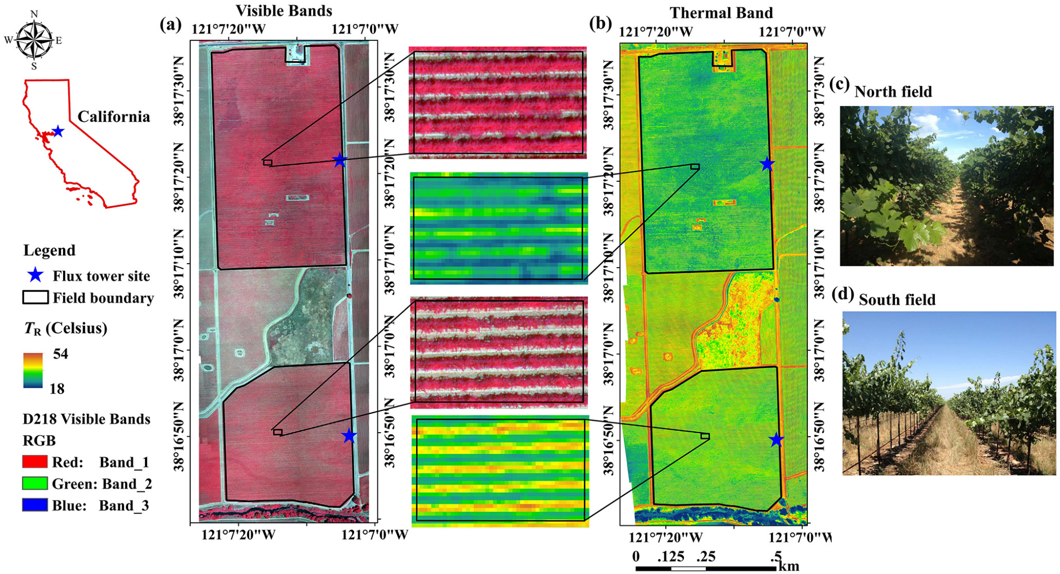

Figure 1. Location of study area overlaid on a false color composite of near-infrared (NIR), red, and green bands with 0.1 m spatial resolution **(a)** and thermal band with 0.66 m spatial resolution **(b)** obtained by aircraft on 6 August, DOY 218, 2013. In the visible band image **(a)**, red and gray colors denote the vine and bare soil/senescent cover crop in the inter-row, respectively, while in the thermal band image **(b)**, blue/green and yellow/red colors represent vine and bare soil/senescent cover crop in the inter-row, respectively. The black line denotes the boundary of north and south fields, and the blue stars are the locations of the flux tower sites. The two photos of the north and south fields (**c** and **d**) were taken on 11 June 2014 after vines had fully leafed out.

HESSD
12, 11905–11957, 2015

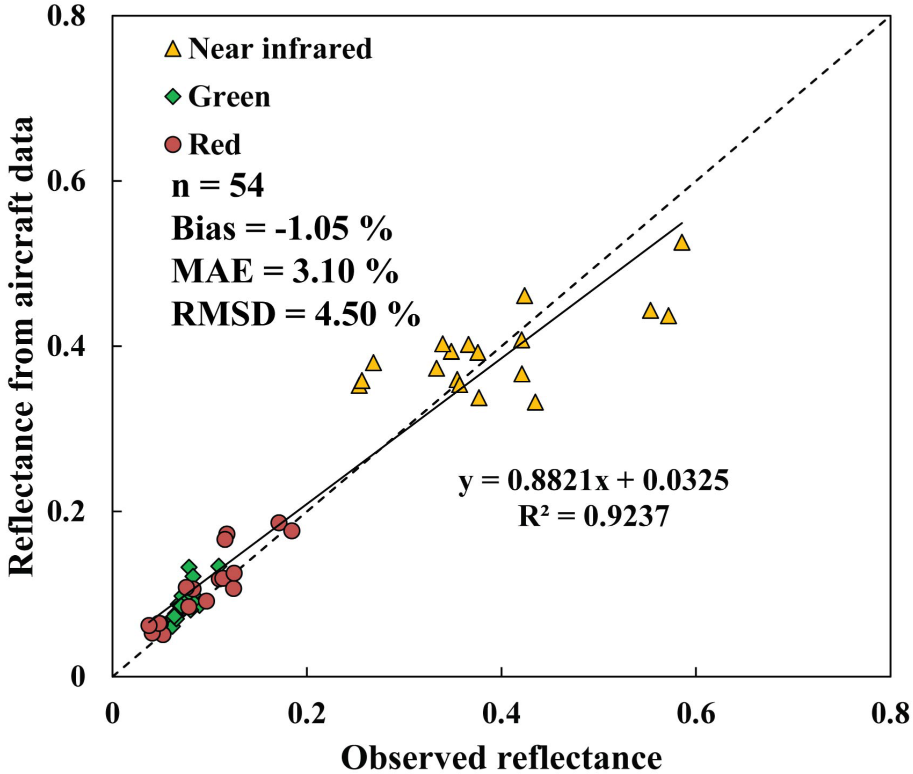

Figure 2. Comparison between observed (O) and modeled (M) visible band reflectance. The statistics (for the sample size $n = 54$) listed in the figure are the Bias ($\Sigma(O-M)/n$), mean absolute error (MAE = $\Sigma|O-M|/n$) and root mean square difference (RMSD = $[\Sigma(O-M)^2/n]^{1/2}$) where Σ represents summation.

HESSD
12, 11905–11957, 2015

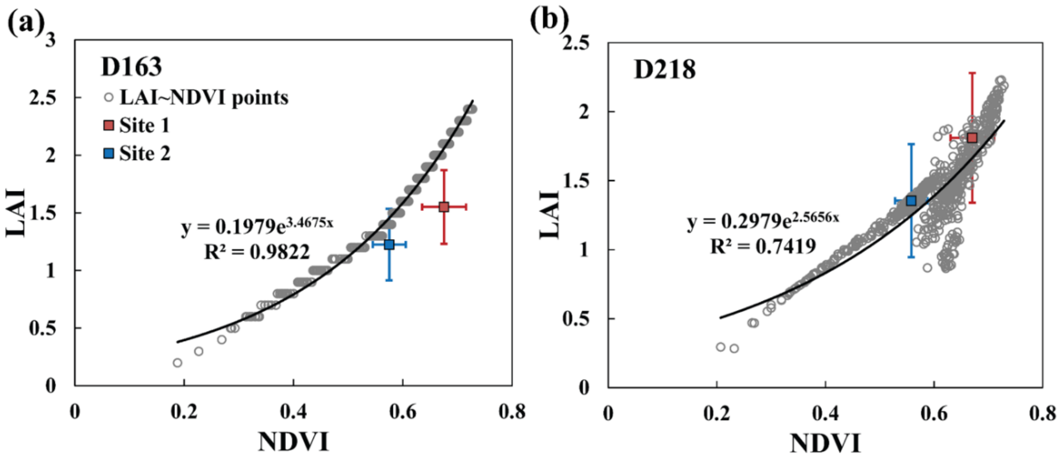

Figure 3. Validation of the LAI ~ NDVI relation using the ground-based LAI measurements on DOY 163 and 218.

HESSD
12, 11905–11957, 2015

Mapping evapotranspiration with high resolution aircraft imagery

T. Xia et al.

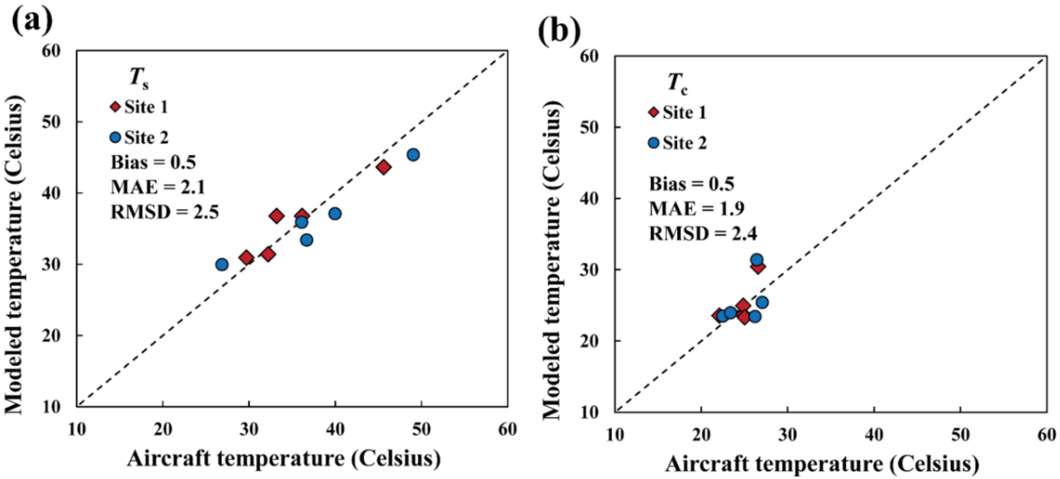

Figure 4. Comparison between modeled T_s and T_c from TSEB and values extracted from the aircraft imagery on the five acquisition days. All the statistics (Bias, MAE and RMSD) have units of °C.

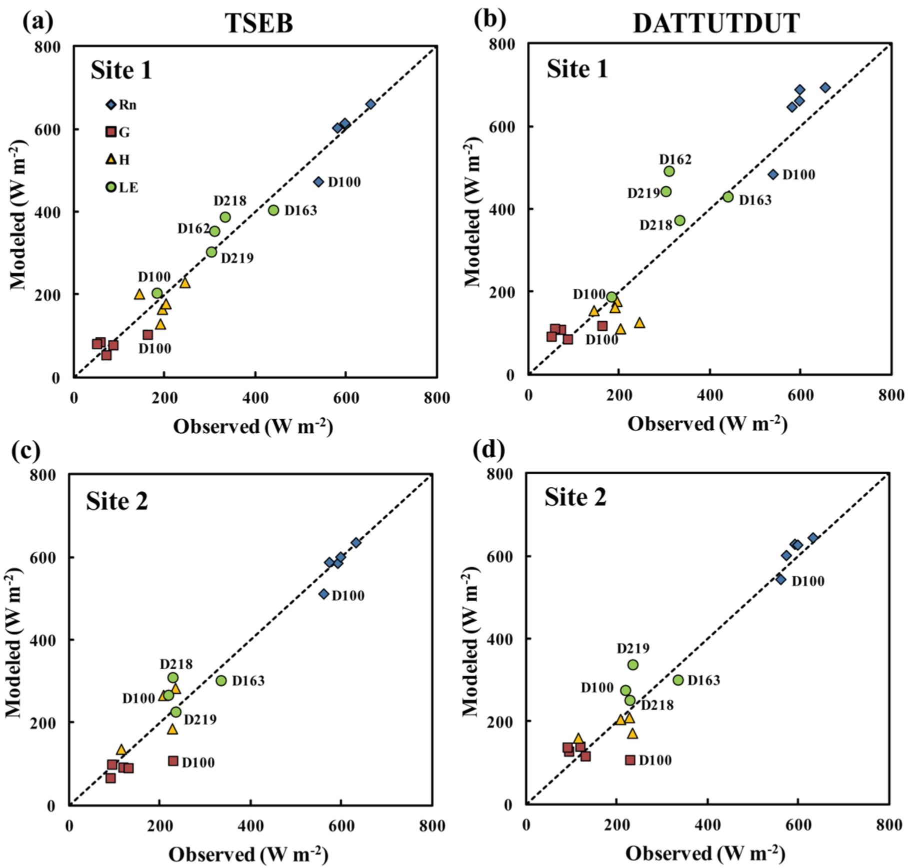

Figure 5. Scatter plot of observed and modeled fluxes from TSEB and DATTUTDUT at the aircraft overpass time for the five days in 2013. The observed *H* and LE use the RE method for energy balance closure. Note for DOY 162, there were no flux data from Site 2 due to an EC sensor malfunction.

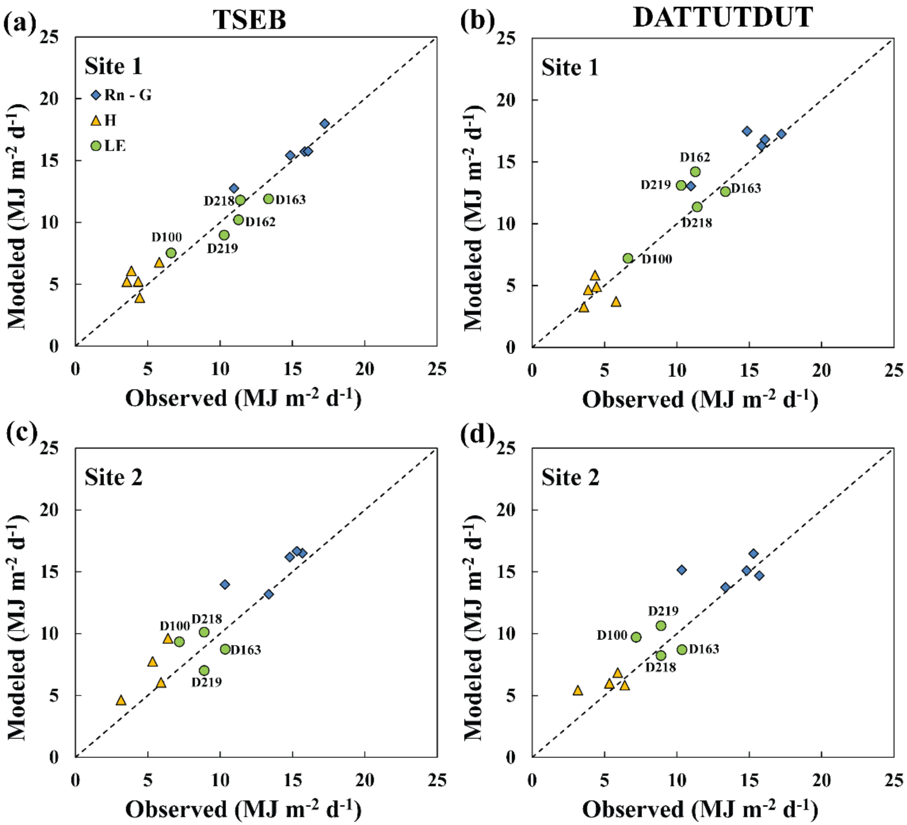

Figure 6. Scatter plot of observed and modeled daytime fluxes from TSEB and DATTUTDUT model at daytime timesteps for the five days in 2013. The observed energy components are adjusted for energy balance using the RE method.

HESSD
12, 11905–11957, 2015

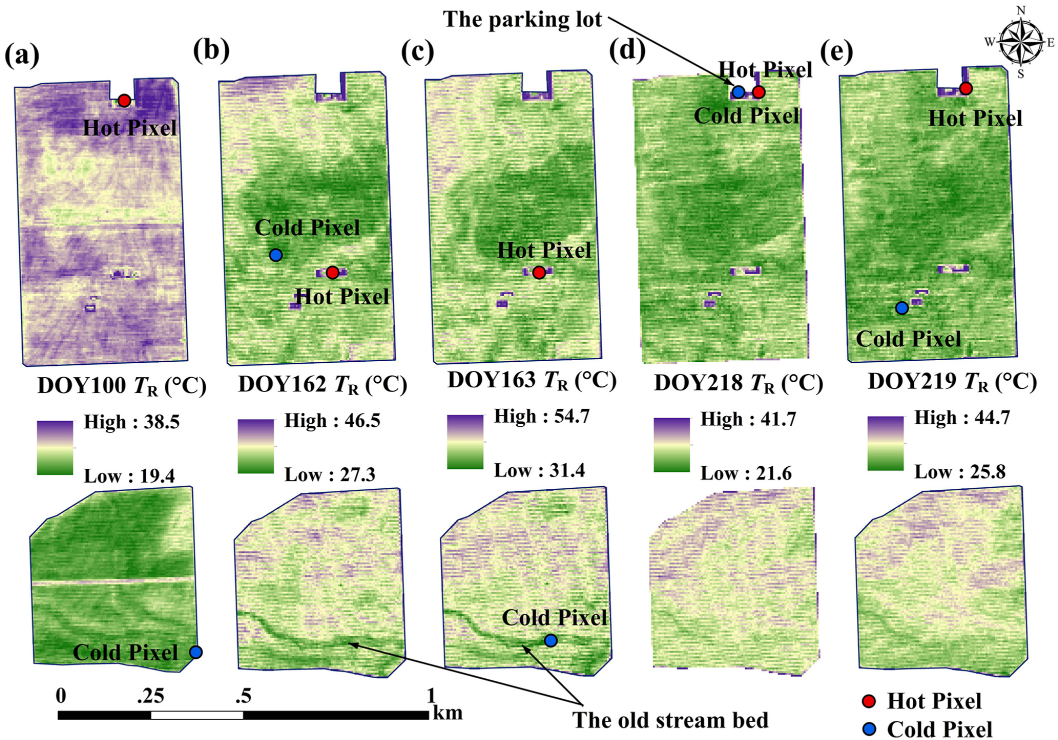

Figure 7. Locations of hot (red points) and cold (blue points) pixels selected from the T_R maps for DATTUTDUT model on the five days.

HESSD
12, 11905–11957, 2015

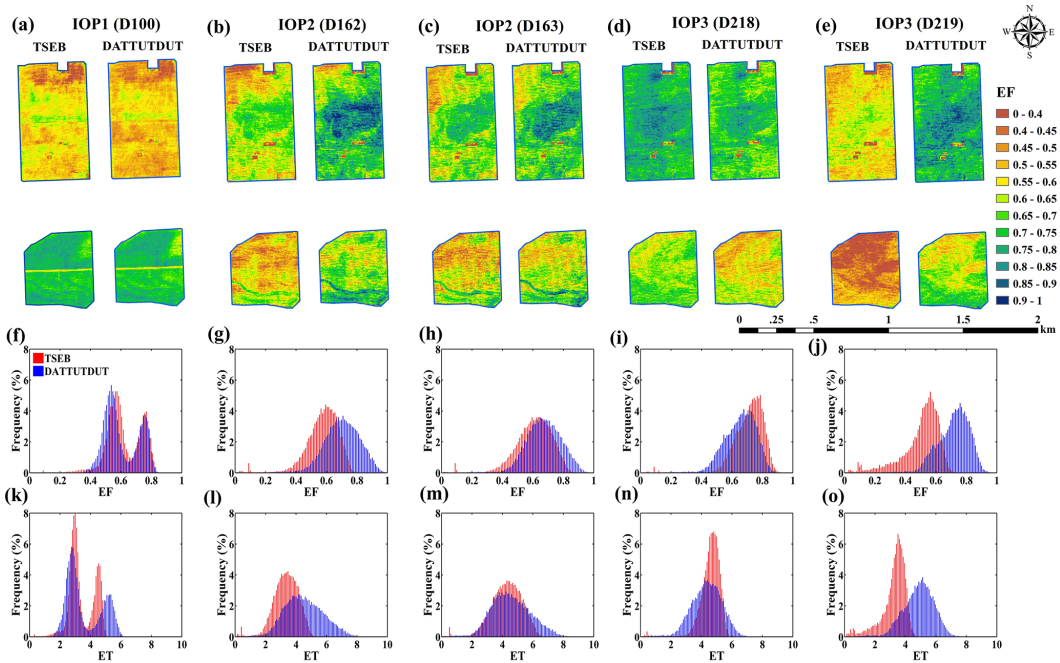

Figure 8. Comparison of TSEB and DATTUTDUT model output: spatial distribution of instantaneous EF (**a** to **e**), frequency histogram of instantaneous EF (**f** to **j**) and daytime ET (**k** to **o**).

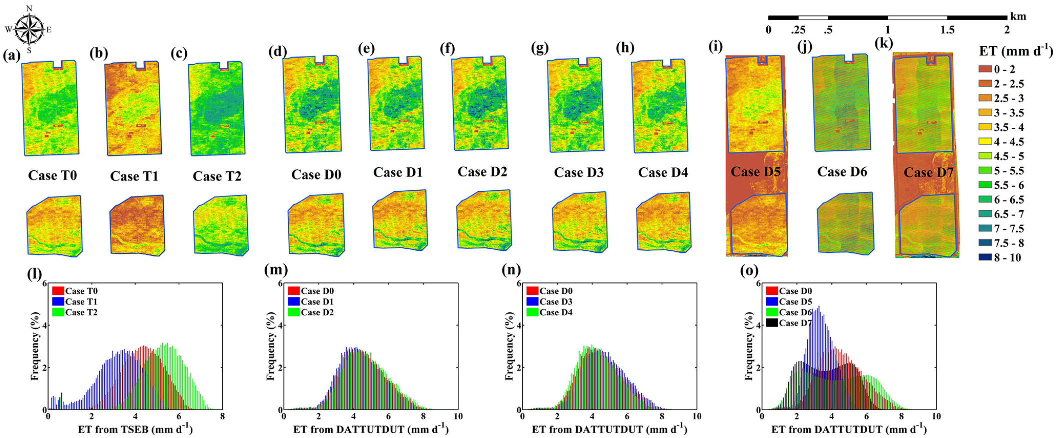

Figure 9. Comparison of the ET patterns and frequency distributions generated by TSEB and DATTUTDUT under the sensitivity tests described in Table 4.

HESSD
12, 11905–11957, 2015

Mapping evapotranspiration with high resolution aircraft imagery

T. Xia et al.

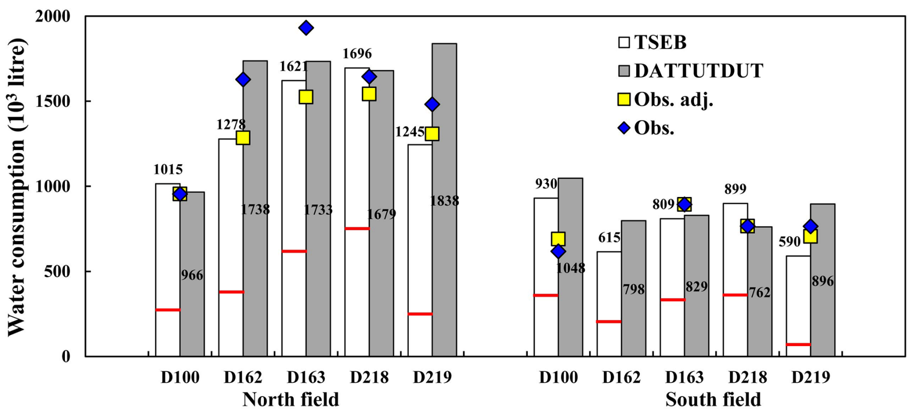

Figure 10. Water consumption calculated from estimates of ET computed by TSEB and DATTUTDUT models for the five aircraft overpass days (10^3 L). The numerical values above or in the columns denote the total water consumption from each field as estimated by the two models. For results from TSEB, the red lines separate the total water consumption into soil evaporation below the lines and vegetation transpiration above the lines. The blue diamonds denote the water consumption calculated using the EC tower-based daytime ET observed (Obs.) multiplied by the area of the north and south vineyards. The yellow squares are the water consumption values from ET Obs. adjusted (adj.) by multiplying ET Obs. by the ratio of the tower source area LAI and the whole field average LAI.

HESSD
12, 11905–11957, 2015

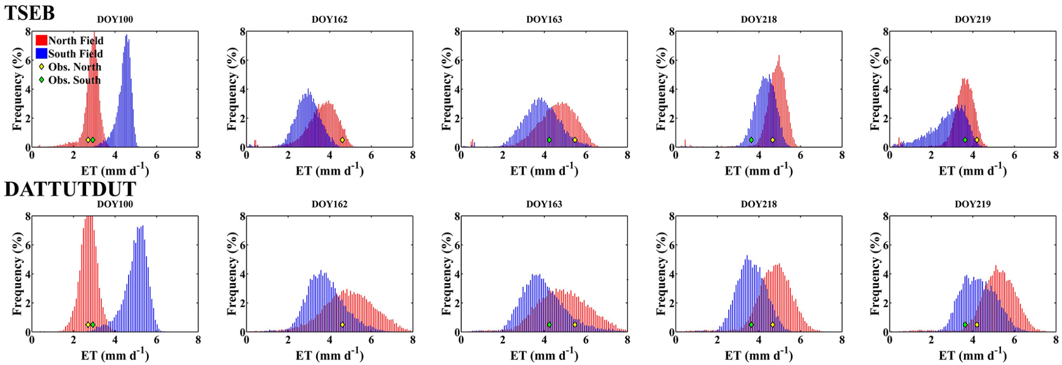

Figure 11. Histograms of output of spatially distributed daytime ET estimated from the TSEB and DATTUTDUT with the daytime ET values from the flux towers identified in the distributions by a yellow and green diamond for the north and south vineyards, respectively.